# Unifying natural and laboratory chemical weathering with interfacial dissolution-reprecipitation: a study based on the nanometer-scale chemistry of fluid-silicate interfaces

Roland Hellmann[1†], Richard Wirth[2], Damien Daval[3], Jean-Paul Barnes[4], Jean-Michel Penisson[5*], Delphine Tisserand[1], Thierry Epicier[6], Brigitte Florin[4], & Richard L. Hervig[7]

[1] *ISTerre, University of Grenoble 1, Observatory for Earth and Space Sciences (OSUG), F-38041 Grenoble Cedex 9, France*

[2] *GeoForschungsZentrum Potsdam, Telegrafenberg, D-14482 Potsdam, Germany*

[3] *Earth Sciences Division, Lawrence Berkeley National Laboratory, Berkeley, California, 94720 USA*

[4] *CEA-Leti, MINATEC Campus, 17 rue des Martyrs, 38054 Grenoble Cedex 9, France*

[5] *DRFMC, CEA Grenoble, F-38054 Grenoble Cedex 9, France*

[6] *INSA Lyon - MATEIS: UMR CNRS 5510, F-69621 Villeurbanne Cedex, France*

[7] School of Earth and Space Exploration, Arizona State University, Tempe, Arizona, 85287-1404 USA

* (retired)

† roland.hellmann@obs.ujf-grenoble.fr

Manuscript submitted to *Chemical Geology*

Formatiert

Formatiert

Formatiert

Formatiert

Formatiert

Formatiert

Formatiert

## ABSTRACT

Chemical weathering reactions of rocks at Earth's surface play a major role in the chemical cycle of elements, and represent one of the major abiotic sinks for atmospheric $CO_2$. Because natural chemical weathering reactions occur at different and more complex chemical conditions than laboratory-based weathering experiments, it has long been thought that the underlying fluid-mineral interaction mechanisms are different. In contrast to most previous studies that have relied on ion, electron, and X-ray beam techniques (characterized by μm to mm lateral spatial resolution) to obtain chemical depth profiles of altered mineral surfaces, we have used high resolution and energy filtered transmission electron microscopy (HRTEM, EFTEM) to study mineral-fluid interfaces using TEM foils cut directly across the reaction boundaries. This allowed measurements to be made directly in cross section at nanometer to sub-nanometer-resolution. Our measurements of the surface chemistry and structure of a large suite of laboratory-altered and field-weathered silicate minerals indicate the general presence of surface layers composed of amorphous, hydrated silica. In each case, the boundary between the parent mineral and the corresponding silica layer is characterized by sharp, nanometer-scale chemical concentration jumps that are spatially coincident with a very sharp crystalline-amorphous interfacial boundary. TEM, atomic force microscopy (AFM), and aqueous chemistry data suggest that the surface layers are permeable to fluids. Taken together, our measurements are not in agreement with currently accepted models for chemical weathering, in particular the leached layer theory. Most importantly, our data provide critical evidence for a single mechanism based on interfacial dissolution-reprecipitation. This concept not only unifies weathering processes for the first time, but we also suggest that nanoscale-surface processes can have a potentially negative impact on $CO_2$ uptake associated with chemical weathering. The results in this study, when combined with recently published research on fluid-assisted mineral replacement reactions, supports the idea that dissolution-reprecipitation is a universal mechanism controlling fluid-mineral interactions (Putnis and Putnis, 2007). Based on this we propose the existence of a chemical weathering continuum based solely on the interfacial dissolution-reprecipitation mechanism.

**Keywords:** chemical weathering, dissolution-reprecipitation, silicate minerals, transmission electron microscopy (TEM), fluid-solid interfaces, $CO_2$ sequestration

## 1. Introduction

### 1.1. *Overview of laboratory and natural chemical weathering processes*

Chemical weathering reactions control in large part the chemical cycle of elements in surface and near-surface environments, chemical denudation rates, the quality of potable water resources (e.g., arsenic in SE Asia), soil formation and nutrient availability, and ore genesis. Moreover, the two major abiotic processes that regulate atmospheric $CO_2$ drawdown are $CO_2$ uptake in oceans and $CO_2$ consumption by chemical weathering reactions. Geological radwaste and $CO_2$ storage are just two examples where weathering processes play a key role in current environmental issues. Because of its global and multidisciplinary importance, chemical weathering has been the subject of laboratory research for more than a century now. However, there is a long-standing assumption that the mechanism(s) controlling weathering in the field are far different from those that operate in simple laboratory experiments. For example, Hochella and Banfield (1995) conceptualize these differences in terms of a broad continuum: one pole is defined by laboratory dissolution reactions (and in some cases natural weathering) that start out being incongruent due to preferential ion exchange, evolve to congruency, and are characterized by the general suppression of secondary phases; at the other end of the continuum are natural weathering reactions that are inherently incongruent overall and occur via direct structural transformation of primary into secondary mineral phases.

In this study we resolve this long-standing controversy by demonstrating that despite differences in environmental and chemical complexity, both field and laboratory weathering are controlled by a single unifying mechanism: interfacial dissolution-reprecipitation. Here, reprecipitation refers strictly to an interfacial process that leads to the formation of amorphous hydrated silica layers on primary silicate mineral surfaces, irrespective of the degree of chemical saturation of the associated bulk solutions with respect to all silica polymorphs. Subsequent precipitation of oxides, oxyhydroxides, and clays from chemically saturated bulk solutions, while evidently playing an important role in weathering processes, are not

specifically addressed in this study. Chemical weathering experiments in the laboratory, both in the past and at present, generally involve chemically dilute, undersaturated solutions at temperatures below 100 °C in acid to circum-neutral pH solutions (see extensive compilation in Bandstra et al., 2008; older compilations in Blum and Stillings, 1995; Brantley, 2003). In laboratory studies at acid to circum-neutral pH, multi-cation silicates are characterized by the apparent non-stoichiometric, preferential release of interstitial cations, as well as Al (Garrels and Howard, 1957; Wollast, 1967; Luce et al., 1972; Paces, 1973; Chou and Wollast, 1985; Muir et al., 1989, 1990; Inskeep, 1991; Hellmann, 1994, 1995; Schweda et al., 1997; Lee et al., 2008; Kameda et al., 2009), leading to the formation of chemically distinct surface altered zones, commonly called 'leached layers'. Based on both aqueous data and surface sensitive analytical techniques, it is thought that the leached layer mechanism is primarily controlled by two separate processes operating simultaneously (schematically shown in Fig.1):

a. charged-balanced, ion exchange via solid-state volume interdiffusion of cations from the mineral with protons ($H^+$ or $H_3O^+$) from the bulk solution (e.g. Garrels and Howard, 1957; Wollast, 1967; Luce et al., 1967; Paces, 1973; Muir et al., 1988, 1989; Casey et al., 1988; Petit et al., 1989; Casey and Bunker, 1990; Banfield et al., 1995; Hellmann, 1997; Hellmann et al., 1997; Schweda et al., 1997; Yang et al., 2009) (possibly accompanied by the inward diffusion of water- see Petit et al., 1990)

b. chemical hydrolysis reactions release Si and O into the bulk solution at the outer interface (Casey et al., 1988, 1993; Petit et al., 1989; Banfield et al., 1995; Hellmann, 1995; Schweda, 1990; Yang et al., 2009).

The rate of retreat of the parent mineral at the inner interface of the leached layer is controlled by process *a*, whereas process *b* controls the rate of retreat of the external interface. Once rates *a* and *b* become equal, a steady-state thickness is achieved.

It is also postulated that leached layers can undergo molecular-scale reorganization, such as repolymerization (also called recondensation) reactions of silanol groups (Casey and Bunker, 1990; Arnold et al., 1992; Casey et al., 1993; Hellmann et al., 1997; Schweda et al., 1997) created by the preferential release of cations (i.e., $\equiv Si-OH + HO-Si\equiv \rightarrow \equiv Si-O-Si\equiv + H_2O$), recrystallization (Banfield et al., 1995), restructuring (Casey et al., 1993; Tsomaia et al., 2003), structural collapse (Paces, 1973), and

even porosity creation (Casey and Bunker, 1990). In particular, much work on restructuring processes in surface (altered) layers has been carried out in glass studies (Pederson et al., 1985; Bunker et al., 1988; Casey and Bunker, 1990; Cailleteau et al., 2008). In addition, silica back reactions, as well as readsorption of silica (Banfield et al., 1995), have also been proposed to occur within leached layers.

The more than 50 year-old leached layer theory remains the currently accepted concept for explaining the apparent non-stoichiometric chemical weathering of minerals, as well as glasses. It is interesting to note that the concepts of leached layer formation, as described in recent reviews of mineral and glass dissolution, have not strayed from the classical ideas detailed above (see e.g., Brantley, 2008; Ohlin et al., 2010). Nonetheless, a few studies of laboratory weathering have questioned this theory. To cite just one example, Teng et al. (2001), using X-ray reflectivity and AFM, attributed the apparent non-stoichiometry of orthoclase dissolution to the formation of a surface silica gel.

In contrast to laboratory studies, chemical weathering reactions of rocks on the Earth's surface and near surface are noted for their chemical and environmental complexity. The chemical saturation states of natural waters and soil pore fluids are extremely variable (Stefánsson and Arnórsson, 2000; Maher et al., 2009). Moreover, the chemistry of natural aqueous solutions is complex, and can include the presence of free metal cations, ligand complexing agents, humic substances, and naturally occurring organic and inorganic acids (Drever, 2003). Mineral grains subject to weathering reactions also do not have pristine surfaces (as in laboratory experiments), since they are often covered with mineral coatings (Nugent et al., 1998; Kawano and Tomita, 2001; Dixon et al., 2002) or clay minerals (Banfield and Eggleton, 1990; Nugent et al., 1998; Zhu et al., 2006). In the critical zone, biota (Barker et al., 1998; Berner et al., 2003; Bonneville et al, 2009) can also adhere to and even penetrate mineral surfaces, thereby directly affecting the dissolution process.

Largely because natural chemical weathering is more complex, there is no unanimity with respect to an intrinsic mechanism (Nesbitt and Muir, 1988; Hochella and Banfield, 1995; Seyama and Soma, 2003; Zhu et al., 2006; see also Table 1 in Lee et al., 2008). Studies advocating leached layers show Si-rich, cation-depleted surface altered layers on naturally weathered minerals (Nesbitt and Muir, 1988; Mogk, 1990; Banfield and Eggleton, 1990;

Nugent et al., 1998; Kawano and Tomita, 2001; Zhu et al., 2006). Several of these studies document sigmoidal cation depletion profiles (Nugent et al., 1998; Nesbitt and Muir, 1988; Mogk, 1990; see also review by Chardon et al., 2006). Alternatively, other studies have failed to find unambiguous evidence for important surface alteration (i.e., very thin surface layers, estimated to be < 2-3 nm in thickness; e.g. Berner and Holdren, 1977; Teng et al., 2001; Lee et al., 2007, 2008), or revealing only clays and/or other neo-formed mineral coatings on the surface (Berner and Holdren, 1977; 1979; Banfield et al., 1995; Dixon et al., 2002). And finally, surface chemical weathering reactions, as well as water-rock interactions at elevated temperature and pressure conditions, can also occur by mineral replacement, which is defined as the direct replacement of a primary mineral by another mineral (Parsons, 1978; Banfield and Eggleton, 1990; Banfield et al., 1995; Lee and Parsons, 1998; Fiebig and Hoefs, 2002; Harlov et al., 2002; Harlov and Förster, 2003; Labotka et al., 2004; Perez and Boles, 2005; Geisler et al., 2007; see reviews in Hochella and Banfield, 1995; Putnis, 2009). Whether mineral replacement occurs directly by solid-state structural transformation, interdiffusion of cations with aqueous species, or surface chemical reactions may be a function of the sample investigated and the analytical technique applied, and therefore remains a subject of ongoing research.

In the present investigation we studied chemical weathering by examining the nanoscale changes in the structure and chemistry of altered silicate mineral surfaces using focused ion beam milling (FIB) to prepare electron transparent foils of uniform thickness across the reaction boundaries. This permitted the altered mineral surfaces to be structurally and chemically characterized *directly in cross section* using high resolution transmission electron microscopy (HRTEM), energy filtered TEM (EFTEM), high angle annular dark field scanning TEM (STEM-HAADF), and energy dispersive X-ray analysis (EDX). Crucial to our study was EFTEM since it provided chemical maps at 1 nm-spatial resolution.

While many previous studies have used TEM to document structural modifications of altered mineral surfaces (e.g. Banfield and Eggleton, 1990; Casey et al., 1993; Banfield et al., 1995; Kawano and Tomita, 2001; Zhu et al., 2006; see also review in Hochella and Banfield, 1995), the concomitant changes in chemistry of the surface altered layers were not integrally measured with nanometer spatial resolution, or alternatively, were measured indirectly with

surface incident ion, electron, or X-ray beam techniques that have intrinsically poor lateral spatial resolution (i.e., μm to mm-scale beams). The use of these techniques can result in artificially broadened cation depth profiles (Hellmann et al., 2003; 2004), which in turn can lead to erroneous interpretations with respect to mineral weathering mechanisms. To circumvent these analytical problems, Hellmann and co-authors (2003) used a new methodology, based on a combination of ultramicrotomy and EFTEM, to measure in *cross section* the near-surface chemistry of surface layers on a feldspar. Their surprising and unique set of nano-scale chemical maps and profiles led them to propose that the silica surface layers could best be explained by an interfacial dissolution-reprecipitation mechanism. Furthermore, their results were inconsistent with interdiffusion and leached layer formation.

1.2. *Development of dissolution-reprecipitation concept*

In the early 50's, significant research was being devoted to understanding feldspar-feldspar transformation reactions. For example, Goldsmith and Laves (1954) studied the isochemical conversion of microcline (triclinic; disordered distribution of Al, Si) to sanidine (monoclinic, ordered distribution of Al, Si). They argued for a 'classical' solid-state diffusive transfer of Si and Al at dry conditions and elevated temperatures, but alternatively, at hydrothermal conditions, they proposed a process comprising the dissolution of microcline and reprecipitation of sanidine. In another study, Wyart and Sabatier (1958) showed that the hydrothermal alteration of labradorite in $KCl_{aq}$ led to the formation of distinct, crystallographic domains of orthoclase and anorthite, which requires the rapid migration of Al and Si. To explain this, these authors hinted at the possibility of a dissolution-reprecipitation process, but in the end, they argued for a solid-state diffusion process catalyzed by water. Nonetheless, these authors were perplexed at how water could have this effect without penetrating the crystal structure. Research on oxygen mobility in hydrothermally-altered K-feldspars led Mérigoux (1968) to propose that dissolution-reprecipitation best explains the rapid incorporation of $^{18}O$ into a secondary Na-feldspar phase.

The pioneering research of O'Neil and Taylor (1967) provided a real conceptual breakthrough in this domain- they suggested interfacial dissolution-reprecipitation as an alternative mechanism to 'atom-for-atom exchange by solid state diffusion' to explain K feldspar-Na feldspar mineral replacement under hydrothermal conditions. Most importantly,

209 they argued that a ‘reaction front sweeps through each crystal grain’, and that the reaction
210 front is associated with a thin fluid film at the interface between the exchanged and
211 unexchanged feldspar. Parsons (1978) suggested that the crystallographic transformation of
212 orthoclase to microcline in plutonic rocks may also occur via the mechanism proposed by
213 O’Neill and Taylor (1967).

214 Nonetheless, until recently this mechanism has remained an unproven concept because
215 sharp chemical fronts could not be measured analytically at high spatial resolution. However,
216 this changed with the advent of new nano-scale chemical imaging techniques, in particular
217 EFTEM and EELS, as well as high-resolution (50-100 nm) isotope tracer ($^{18}O$)
218 measurements. This has led to far-reaching advances in the understanding of fluid-solid
219 interfacial processes occurring both in the laboratory and in the field during chemical
220 weathering of minerals (Hellmann et al., 2003, 2004; Daval et al., 2011; King et al., 2011)
221 and mineral replacement reactions (e.g. Fiebig and Hoefs, 2002; Lobatka et al., 2004; Putnis
222 and Mezger, 2004; Putnis et al., 2005; Harlov et al., 2002, 2005; Harlov and Förster, 2003;
223 Geisler et al., 2007; Hövelmann et al., 2010; see also extensive reviews in Putnis, 2002,
224 2009). Even the glass dissolution field has seen important advances with the application of
225 these new techniques (Geisler et al, 2010).

226 The significance of the present study is that it extends the preliminary results of
227 Hellmann and co-workers (2003, 2004) with an investigation of a large suite of silicate
228 minerals, altered both in the laboratory and under natural conditions. One of the most
229 important results is that we find unambiguous evidence for just one mechanism, irrespective
230 of whether chemical weathering occurs in the laboratory or in the field. Thus, our findings
231 serve to unify chemical weathering with a single mechanism, interfacial dissolution
232 reprecipitation. Very importantly, the results we present ask for a re-interpretation of a great
233 deal of existing work on chemical weathering, and demand a critical re-evaluation of the old
234 interdiffusion-leached layer model and the general concept of how chemical weathering
235 works.

236 To avoid confusion for the reader, throughout the remainder of the manuscript we use
237 the term ‘surface layers’ to specifically imply the in situ formation of secondary phases (i.e.
238 amorphous silica) on primary mineral surfaces by interfacial dissolution-reprecipitation.

Alternatively, use of the term 'surface altered layers' refers to the chemical and structural modification of the original mineral lattice, resulting in 'leached layers'. And finally, when no specific mechanism is implied, we use the term 'surface (altered) layers'.

## 2. Materials and Methods

### *2.1. Laboratory chemical weathering*

Using laboratory dissolution experiments we investigated an extensive group of primary silicate minerals having different compositions and structures: the 3-D framework tectosilicates: plagioclase feldspar series (albite: $NaAlSi_3O_8$, labradorite: $Na_{0.39}Ca_{0.59}Al_{1.59}Si_{2.41}O_8$, anorthite: $CaAl_2Si_2O_8$); single chain inosilicates: diopside: $CaMg(SiO_3)_2$, wollastonite: $CaSiO_3$; nesosilicates (isolated $SiO_4$ tetrahedra): pyrope garnet: $Mg_{1.982}\ Ca_{0.372}\ Fe_{0.668}Al_{1.812}\ Cr_{0.118}Si_{3.023}O_{12}$, forsterite olivine: $Fe_{0.168}Mg_{1.796}SiO_4$. Cleaved mineral samples, on the order of several $mm^2$, were hydrolyzed at ambient temperature (~25 °C) and 1 bar over periods of 2-4 weeks in flow-through systems at far-from-equilibrium conditions; the majority was altered in acidic pH solutions ($HCl/H_2O$) at pH 1-3. In general, acid pH conditions were privileged in order to create surface (altered) layers suitably thick for study. Chemical weathering at acid pH conditions (pH 1-3) occurs in many natural environments, such as acid mine drainage sites, hydrothermal volcanic terranes, soils in water sheds subject to acid rainfall, and geological $CO_2$ storage and sequestration sites. Labradorite feldspar was dissolved over a wider range in pH, from 1 to 13 ($KOH/H_2O$ used at basic pH). Surface (altered) layers developed on labradorite at all pHs, but were thinner in the neutral to basic pH range. The cation release rates were measured as a function of time during all of the mineral dissolution experiments. The bulk solutions were always highly undersaturated with respect to potential secondary Si and Al-bearing phases.

### *2.2 Aqueous chemistry*

Aqueous samples were collected at discrete time intervals for all flow experiments. Cation concentrations were determined using inductively coupled plasma-atomic emission spectrometry (ICP-AES) and colorimetry (Si only). All of the minerals displayed initial periods of apparent non-stoichiometric cation release over the first 1-10 days, except for

wollastonite where dissolution remained non-stoichiometric over the duration of hydrolysis (up to 24 d). Steady-state rates were achieved in all runs. The concentration data were converted to individual cation release rates that were stoichiometrically-normalized with respect to each parent mineral (Hellmann, 1994, 1995). These release rates reflect the global dissolution process (net sum of source and sink processes), and are not always equal to the true intrinsic rate of detachment from the original mineral structure. For each mineral, the cation-specific release rates provided complementary information on the relative thickness and composition of the surface (altered) layer. Solution saturation states (Gibbs free energy of reaction) with respect to the primary silicate minerals and possible secondary phases were calculated with the code EQ3NR (Wolery, 1992), using the LLNL 'composite' (com) database and the B-dot equation for activity coefficients of aqueous species. Future publications devoted to each individual mineral will include the corresponding aqueous data and derived rates.

*2.3 Sample preparation*

Samples were rinsed in alcohol and dried under ambient conditions after each experiment, or after collection in the field. Focused ion beam milling (FIB) was used to prepare electron transparent foils of uniform thickness, such that the altered mineral surfaces could be structurally and chemically characterized *directly in cross section* using high resolution TEM techniques. The specific protocol that we used consisted of a. sputter coating a protective 50 to 80 nm-thick layer of carbon or gold on the predominant altered cleavage surface, b. in situ preparation of an electron transparent TEM foil (~80 nm thick) by FIB milling perpendicular (vertical) to the altered surface (for more details on FIB, see Wirth, 2004, 2009), c. placement of foil on holey carbon TEM grid.

An important issue with FIB-TEM foil preparation is the implantation of Pt and Ga into the specimen, which potentially creates artifacts (in particular, amorphization; see, e.g. Lee et al., 2007). We addressed this issue by preparing non-altered mineral specimens as controls to identify potential FIB-produced artifacts, such as amorphization or altered chemistry. In addition, routine Ga and Pt EDX line scans across thin surface (altered) layers (e.g. garnet, olivine, diopside) showed these elements to be merely present at the limits of detection.

299 Moreover, even with respect to the thinnest surface layers investigated in this study (≤ 5 nm,
300 diopside and olivine), HRTEM and EFTEM/EDX, respectively, showed no evidence for local
301 amorphization or changes in the chemistry in the unaltered parent mineral adjacent to the
302 surface layer. Our aqueous chemistry results also provided an independent control on the
303 chemistry and thicknesses of the surface (altered) layers. Based on these criteria, we are
304 confident of the efficacy of the protective C and Au coatings used.
305 For each laboratory-altered mineral specimen, the FIB-prepared TEM foils were cut
306 perpendicular to the indicated prominent cleavage or parting planes (number of individual
307 specimens analyzed by TEM also indicated): albite {010}: 3; anorthite {010}: 1; labradorite
308 {010}: 7; diopside {110}: 4; wollastonite {100}: 3; olivine {not determined}: 2; garnet
309 {110}: 3. With respect to the naturally weathered K-feldspar {not determined}:3 and
310 serpentine-lizardite {not determined}: 5, we simply chose prominent flat (weathered)
311 cleavage surfaces under an optical microscope; these same surfaces were then milled by FIB
312 perpendicular to the surface to obtain the cross-sectional ultra-thin sections that were
313 subsequently examined by TEM.
314

315 *2.4. Solid-state analyses*

316 On each FIB-prepared foil, five to ten different areas of the surface layer were
317 investigated by TEM. Electron irradiation damage was mitigated by first orienting each
318 sample and then recording images and data as fast as possible in adjacent pristine regions;
319 EFTEM and EDX counting times were kept to a minimum to avoid electron beam induced
320 diffusion of mobile elements. Because of the large scope of the study, a total of 4
321 TEM/laboratories were used (moreover, the choice of instruments was dictated by the
322 technical characteristics of each TEM, in particular, TEM-FEG was used for high resolution
323 EDX line scans): GFZ Potsdam- Philips CM 200 ($LaB_6$) operated at 200 kV, EDAX Si-Li
324 detector with ultra-thin window; CEA LETI-Minatec Grenoble: Jeol JEM 2010FEF (FEG)
325 operated at 200 kV, 1 nm FWHM spot size, EDX detector: Oxford-Inca Si-Li analyzer with
326 an ultra-thin window; CEA Grenoble- Jeol 3010 ($LaB_6$) operated at 300 kV, energy dispersion
327 = 0.2 eV/channel, collection angle $\beta$ = 6.5 mrad; INSA (CLYM) Lyon - Jeol 2010 (FEG)
328 operated at 200kV, with EDX analyses based on 2.4 and 1.0 nm probe sizes using an Oxford-

Inca Si-Li analyzer with an ultra-thin window. FEG-SEM-EDX analyses (serpentine only) were obtained using a Hitachi S-5500 operated at 30 kV (EDX Noran ThermoScientific silicone drift detector), CEA-LETI Grenoble. EFTEM chemical images and EEL spectra were obtained with a post-column Gatan GIF (GFZ, CEA Grenoble) or an in-column Omega (CEA-LETI-Minatec) imaging filter, using the Ca $L_{2,3}$, O *K*, K *K*, Al *K*, Mg *K*, and Si *K* edges.

EFTEM chemical mapping was based on either the two-window (jump ratio) or three-window (elemental map) method (for details, see Hofer et al., 1997). The energy windows for pre-edge and post-edge images were based on standard settings in the Gatan Digital Micrograph software (typically with a 20 eV slit width). Thickness maps were determined by EELS to verify approximate uniform thicknesses of the FIB thin sections in the areas of interest. All elemental TEM-EDX line scans were obtained using *K*α X-ray intensities. Atomic force microscopy (AFM) was based on a Digital Instruments Dimension 3100, ENSEEG (Univ. Grenoble); images were acquired in tapping mode using a Nanosensors Pointprobe-Plus Silicon SPM sensor. SIMS elemental depth profiles were obtained with a Cameca IMS 3f instrument (ASU) using an $^{16}O^-$ primary ion beam, 25 nA beam current, 12.6 kV accelerating voltage, 125x125 $\mu m^2$ raster area, and ion beam incident at 30° to the sample normal.

### *2.5. Naturally weathered samples collected in field*

We chose to investigate two end-member rock types, a granite and a serpentinite. The granite, with an original provenance from the Mt. Blanc granitic pluton, is a glacial erratic boulder that may have been deposited during the last deglaciation on a limestone plateau (Pte. Andey: 46.039 °N, 6.426 °E, 1600 m elevation; Haute Savoie, France). The boulder has an apparent $^{10}$Be exposure age of 14.7±3.7 ka (note that the true age may be considerably greater depending on assumed surface erosion rate). For this study, we chose to specifically investigate naturally weathered potassium feldspars, which are the primary mineralogical component of these granites. Feldspar grains were either extracted from the surface of the boulder (subaerial weathering) or from a depth of ~20 cm in the underlying adjacent soil. The serpentinite sample was collected in the southern part of the Belledonne Massif (45° 07' 55"

359 N, 5° 54' 52" E; 2000 m elevation, Lac Robert, Chamrousse, near Grenoble, France). The
360 lithology of the Lac Robert area is primarily characterized by amphibolites and serpentinites.
361
362 **3. Results**
363 The most important finding pertaining to all of the laboratory-weathered samples is that
364 the TEM-measured depth profiles show that both the outer and inner interfaces of the surface
365 layers are characterized by sharp (nm-scale), step function-like changes in cation
366 concentrations. The nm-sharp chemical gradients at the inner interfaces are spatially
367 coincident with almost atomically sharp (<2nm) crystalline-amorphous structural transitions.
368 TEM showed all surface layers to be amorphous, less dense, and chemically distinct (silica-
369 rich) compared to the parent minerals, with thicknesses varying from ~5 to 870 nm. In
370 general, the nesosilicates developed the thinnest surface alteration, but in addition, there were
371 significant differences in thickness within single structural groups, e.g. tectosilicates:
372 labradorite >> albite > anorthite; single chain inosilicates: wollastonite >> diopside;
373 nesosilicates: garnet > olivine. This quantification does not take into account the potential
374 effect of anisotropic dissolution with respect to different crystal faces for a given mineral.
375 Figures 2A-C show nanoscale images and chemical maps obtained for surface (altered)
376 layers that formed on three structurally different minerals after weathering in the laboratory:
377 labradorite, wollastonite, and pyrope garnet. The thick surface layer that formed on
378 labradorite at acid pH displays typical features common to all samples: a crystal lattice
379 terminating abruptly at an amorphous surface layer (Fig. 2A-i, ii) enriched in silica and
380 depleted in other cations (e.g. Ca, Al- see EDX profiles in Fig. 2A-i); the EFTEM profiles
381 reveal very sharp chemical gradients (Ca, Fig. 2A-iii; Si, Fig. 2A-iv). The chemical gradients
382 of Ca and Si are opposite in sign, due to Ca depletion vs. Si enrichment. Hydrogen (Fig. 2A-i
383 inset) and boron (not shown) SIMS depth profiles in the altered layer provide evidence that
384 aqueous species from the bulk fluid permeated all the way to the pristine mineral interface.
385 Alteration at circum-neutral pH (4.0 and 5.7) resulted in much thinner surface layers (≤25
386 nm). The other feldspars, namely albite and anorthite, possessed significantly thinner surface
387 layers; e.g., those on anorthite were only 2-5 nm in thickness.

Minerals from the other structural groups developed surface layers with additional chemical and structural complexity. Altered wollastonite reveals high porosity throughout the thick surface layer; there is also evidence for localized physical separation of the surface layer from the parent mineral (Fig. 2B-i), indicating a lack of structural continuity between the two phases. In Fig. 2B-i the EFTEM profiles of Ca and Si reveal, respectively, depletion and enrichment associated with very sharp chemical interfaces. Figure 2B-ii shows an atomic force microscopy (AFM) image of the surface of the precipitated silica. The botryoidal topography and large pores are consistent with elevated internal porosity. Diopside alteration produced 10-20 nm-thick Ca and Mg-depleted surface layers. The most complex surface layers formed during garnet alteration. Although thin, they are characterized by three parallel zones of different density that correlate with generalized cation depletion and Si enrichment, but in addition, also correlate with two narrow zones of localized cation enrichment (inset, Fig. 2C). Olivine surface layers were less complex, and relatively thin ($\leq$ 5 nm).

While the presence of amorphous silica-rich surfaces on naturally weathered silicate minerals is well documented (Banfield and Eggleton, 1990; Kawano and Tomita, 2001; Zhu et al., 2006), we applied the same high spatial resolution chemical mapping techniques to test whether sharp and coincident chemical and structural interfaces also characterize naturally weathered mineral surfaces. Given that the variety of natural weathering environments is tremendously large, for practical reasons we restricted our study to two end-member lithologies (granite, serpentinite) exposed to three distinct weathering environments: mineral-atmosphere, mineral-soil, and mineral-biota.

Several potassium feldspar ($KAlSi_3O_8$) grains from the granite that had undergone either subaerial or intra-soil weathering were investigated. Typical results from both environments show that the feldspar crystal lattice ends abruptly at an amorphous surface layer characterized by a spatially coincident and nm-sharp change in chemistry (K depletion). In Fig. 2D the ~50 nm-thick surface layer is composed of two parallel zones with different densities and K concentrations. In contrast to the laboratory-weathered minerals, this thin amorphous layer is overlain by a variably thick (up to 1-2 μm, not shown) over-coating composed of a silica-rich, amorphous matrix containing abundant phyllosilicates.

417 We also investigated a biota-mineral interface between a several mm-thick, epilithic
418 lichen species (*Rhizocarpon geographicum* gr.) growing subaerially on a serpentinite matrix
419 composed primarily of polycrystalline serpentine (lizardite, $Mg_3Si_2O_5(OH)_4$). Between the
420 lichen and the mineral matrix is a distinct ~150-200 nm-thick amorphous surface layer. The
421 sharp structural boundary between the polycrystalline serpentine and the amorphous layer
422 precisely correlates with an equally sharp change in the chemistry of the layer characterized
423 by both an abrupt increase in Si and depletion in Mg (Fig. 2E).

424 **4. Discussion**

425 The TEM measurements of the field weathered K-feldspar and serpentine demonstrate
426 the natural occurrence of amorphous Si-rich and cation-depleted surface layers having
427 spatially coincident and nm-sharp structural and chemical interfaces. This is indicative of the
428 same weathering mechanism as in the laboratory. The altered K-feldspar revealed additional
429 complexity due to the presence of a thick over-coating on top of the silica layer, which we
430 interpret as a consequence of larger-scale, peripheral chemical weathering (involving abiotic
431 and biotic processes) operating over very long time scales in the presence of fluids at variable,
432 and most probably higher, solution saturation states. These kinds of μm-thick secondary
433 coatings were never observed in our laboratory-weathered samples. In the context of this
434 study, the influence of biota on the overall chemical weathering process remains an open
435 question, as there is no obvious parameter that allows us to discriminate between the effects
436 of abiotic subaerial weathering and lichen-promoted weathering due to, for example, secretion
437 of organic acids.

438 *4.1. Diffusion vs. interfacial dissolution-reprecipitaton*

439 The field and laboratory surface layers we investigated never displayed the smoothly
440 varying, sigmoidal cation concentration profiles that would be predicted for leached layers
441 created by interdiffusion (Fig. 1). An interdiffusion-leached layer mechanism is not
442 compatible with surface layers that display nm-scale step function-like changes in cation
443 concentrations. To confirm this, we modeled the binary interdiffusion of protons and cations
444 using a standard volume interdiffusion equation, based on semi-infinite geometry with a
445 planar, non-stationary (i.e. retreating) fluid-solid interface:

446

$$\frac{\partial C_H}{\partial t} = \frac{\partial}{\partial x}\left( D^* \frac{\partial C_H}{\partial x} \right) + a\frac{\partial C_H}{\partial x} = 0 \qquad (1).$$

In the above expression $C_H$ and $C_{cation}$ are the normalized concentrations of the inward ($H^+$ or $H_3O^+$) and outward diffusing species (note that $C_H = 1 - C_{cation}$), $D^*$ is the binary interdiffusion coefficient, $x$ is the depth into the altered layer measured from the fluid-solid interface, $a$ is the rate of retreat of the fluid-solid (outer) interface (based on experimental rate of Si release), and $\partial C/\partial t = 0$ holds because steady-state conditions were achieved during the experiments. The purpose of the diffusion modeling was to generate theoretical binary cation depletion profiles and compare these to the measured cation depletion profiles on altered labradorite and wollastonite. These minerals were chosen for comparison since they had the thickest surface (altered) layers.

*4.2. Binary interdiffusion of univalent cations with protons*

The binary interdiffusion coefficient is defined as:

$$D^* = \frac{D_H D_{cation}}{C_H D_H + C_{cation} D_{cation}} = \frac{D_H}{1 + bC_H} \qquad (2).$$

where $b = (D_H/D_{cation})-1$. To allow for additional dependence of $D^*$ on chemical and physical changes in the altered layer, $D^*$ can be modified with a depth-dependent structural factor ($\alpha$) (Lanford et al., 1979; Hellmann, 1997), such that $D_\alpha$, a modified form of the interdiffusion coefficient, can be defined as

$$D_\alpha = (1 + \alpha C_H) D^* \qquad (3).$$

Figure 3A shows how the interdiffusion coefficient $D_\alpha$ varies in a highly non-linear manner as a function of cation concentration (i.e. proportional to depth) in the altered layer; this non-linearity reflects much higher diffusion rates at the outer fluid interface compared to the inner interface, a condition that is consistent with the elevated surface micro-porosity we observed by atomic force microscopy, and as indicated by the large uptake of H (see SIMS profile, Fig. 2A-i, inset) adjacent to the fluid-solid interface. Theoretical interdiffusion depth profiles can be obtained by substituting the expression $D_\alpha$ (Eqn. 3) for $D^*$ in Eqn. 2; the modified form of $D^*$ is then substituted into the general diffusion expression (Eqn. 1), which is then solved with the appropriate boundary conditions.

Figure 3B portrays representative cation diffusion profiles based on $\alpha = -0.9$; this value was chosen since it resulted in depth profiles with steep chemical gradients, analogous to those measured. The three sets of diffusion profiles correspond to $a = 10^{-2}$ Å $s^{-1}$ (measured release rate of Si in solution) and values of $D_H = 10^{-16}$, $10^{-15}$, $10^{-14}$ $cm^2s^{-1}$, and for each value of $D_H$, 4 diffusion profiles were calculated corresponding to different ratios of $D_H/D_{cation}$ ($10^{-2}$, $10^{-3}$, $10^{-4}$, $10^{-5}$; note that $D_H/D_{cation} \ll 1$, a condition verified in many glass corrosion studies (e.g. Smets and Lommen, 1982; and references therein). These particular values of $\alpha$, $D_H$, and $D_H/D_{cation}$ were chosen to produce (univalent) cation diffusion profiles that bracket the 400 to 500 nm-thick surface layers that formed on labradorite reacted at acid pH. The profiles based on $-1 < \alpha < -0.9$ are almost indistinguishable from those shown; profiles using $\alpha > -0.9$ reveal an increasing shift to greater depths and less steep (wider) chemical gradients (hence our choice of $\alpha = -0.9$). Overall, the diffusion profiles in Fig. 3B show the influence of the various parameters listed immediately above; in addition, they serve to clarify certain aspects of the binary interdiffusion profiles for di- and trivalent cations discussed below.

Because we were not able to measure the Na profiles in the altered labradorite (due to electron beam migration of Na), a direct comparison with the theoretical univalent cation diffusion profiles in Fig. 3B was not possible. We assumed, however, that the Na profiles should be identical to those of Ca and Al that were measured by EDX and EFTEM (Figs. 2A-i, iii). We made this assumption because the depths of cation depletion in the present study are in perfect accord with those measured at pH 1 on labradorite in Schweda et al., 1997. Moreover, both studies used the exact same starting material (we thank P. Schweda for the pristine labradorite samples). Because Schweda and co-workers used SIMS, their results also show Na profiles, which are identical to the other depleted-cation profiles in their study.

*4.3. Binary interdiffusion of cations ($z = +1,+2,+3$) with protons*

The modeling of binary proton-multivalent cation interdiffusion is more difficult due to the complexity of the $D^*$ term, and thus the existence of an analytical solution remains somewhat speculative. In order to calculate (binary) multi-valence cation (M) depth profiles ($M^{z+}$, with $z = 1$, 2, or 3), a numerical solution was developed. Equation 1 was first integrated assuming steady-state conditions and using the previously mentioned boundary conditions, which leads to the following equation:

$$a = D^*\left(\frac{\partial C}{\partial x}\right) + aC \qquad (4)$$

This equation was then discretized. For an infinitely small interval $\partial x$, Eqn. 4 becomes:

$$C_{i+1} = a \times \Delta x \times (1 - C_i) / D_i^* + C_i \qquad (5)$$

where $C_i$ is the concentration of $M^{z+}$ at depth $x$, $C_{i+1}$ the concentration at depth $x + \Delta x$, and the proton-cation ($M^{z+}$) interdiffusion coefficient is given by:

$$D_i^* = \frac{D_{M^{z+}} D_H \ ((z-1)C_i + 1)}{z^2 D_{M^{z+}} C_i + D_H (1 - C_i)} \qquad (6)$$

In the relation above, $D_H$ and $D_{M^{z+}}$ represent, respectively, the diffusion coefficients of $H^+$ and $M^{z+}$. As was the case for univalent cation interdiffusion, we modified the interdiffusion coefficient with a depth-dependent structural factor, which leads to

$$D_i^* = \left(\frac{D_{M^{z+}} D_H \ ((z-1)C_i + 1)}{z^2 D_{M^{z+}} C_i + D_H (1 - C_i)}\right) \times (1 + \alpha.(1 - C_i)) \qquad (7)$$

We checked our numerical solutions with the cation depth profiles for proton-univalent cation interdiffusion (Fig. 3B), for which an analytical solution exists.

The modeled cation depth profiles ($M^{z+}$, $z$ = 1, 2, 3), shown in Fig. 3C, are based on $D_H = 10^{-16}$, $10^{-15}$, $10^{-14}$ $cm^2s^{-1}$, $D_H/D_{cation} = 10^{-3}$, $a = 10^{-2}$ Å $s^{-1}$, and $\alpha$ = -0.9. These values were chosen to facilitate comparison with the Ca and Al depletion profiles measured for laboratory-altered labradorite. Examination of the modeled diffusion profiles reveals that as $D_H$ increases from $10^{-16}$ to $10^{-14}$ $cm^2s^{-1}$, the cation depth profiles increasingly diverge from one another as a function of valence. The divergence of the diffusion profiles indicates that the depths of cation depletion depend on the valence (depths increase with decreasing valence). This effect is minor at $D_H = 10^{-16}$, but becomes much more pronounced with increasing values of $D_H$ (e.g. $D_H = 10^{-14}$ $cm^2s^{-1}$). Taking the case of $D_H \geq 10^{-14}$ $cm^2s^{-1}$, the depth of depletion of $M^{z+}$ ($z$ = 1) » $M^{z+}$ ($z$ = 3). On the other hand, for a given value of $D_H$, the

534 cation valence does not significantly affect the chemical gradients of the cation depth profiles.
535 Note that in most cases, by simply changing the value of *a* (Eqn. 1), cation depth profiles
536 simulating surface altered layers on other minerals are easily derived in the same manner- e.g.
537 wollastonite.

538 Basing a comparison specifically on labradorite surface alteration, the theoretical
539 binary interdiffusion profiles for $M^{z+}$, $z = 1, 2, 3$ in Fig. 3C can be compared to the 400 nm-
540 thick Ca and Al cation depletion profiles that we measured by EFTEM and EDX (Fig. 2A-i,
541 iii). Two points can be made based on these figures:

542 a. the chemical gradients of the diffusion profiles significantly exceed those measured
543 by EFTEM and EDX, which are sharp on a nanometer-scale
544 b. the modeled binary diffusion profiles indicate a dependence of the depth of cation
545 depletion on cation valence, and yet the measured Ca and Al depth profiles show
546 equal depths of depletion

547 These two points thus show that cation interdiffusion is not consistent with our measured
548 cation depletion profiles. Theoretical diffusion profiles corresponding to ≥500 nm-thick near-
549 surface alteration produced during wollastonite hydrolysis yielded similar results and
550 conclusions.

551 So far we have only considered individual interdiffusion couples for cations of various
552 valences (Fig. 3c). Binary interdiffusion modeling is perfectly adapted to such simple
553 minerals like wollastonite or olivine, as they have only one type of exchangeable cation (i.e.,
554 valence +2). On the other hand, more complex silicate minerals containing multivalent
555 cations (e.g. $Na^{+1}$, $Ca^{+2}$, $Al^{+3}$ in labradorite) may behave differently, given that cations with
556 different valences will interdiffuse simultaneously with protons. The question then becomes
557 whether simultaneous, multi-cation interdiffusion will produce the same diffusion profiles
558 that characterize individual binary interdiffusion profiles. The exact response to this question
559 is unknown, but we would expect that simultaneous diffusion profiles would be steeper than
560 their binary counterparts; in addition, the valence should still play a role in terms of their
561 relative diffusion rates (i.e. the higher the valence, the slower the diffusivity- this yielding
562 shallower depths of cation depletion). Solving the appropriate diffusion equations to account

563 for simultaneous interdiffusion is far from trivial, and to best of our knowledge, has not yet
564 been developed for leached layers.
565
566 *4.4. General conclusions of diffusion modeling*
567 In general, the various binary diffusion scenarios that we present produce smooth,
568 sigmoidal cation depletion profiles (depletion depths of 100-1000 nm), with concentration
569 gradients having widths of many tens to hundreds of nanometers, which is significantly
570 greater than those that we measured. Diffusion modeling reveals that $\alpha$, in conjunction with
571 $D_H$, are the two most important parameters that control both the depths and the gradients of
572 cation depletion. In addition, the cation valence influences the depth of depletion (depending
573 on the value of $D_H$), but has less importance with respect to the chemical gradient. Based on
574 the diffusion model that we used, we conclude that an interdiffusion mechanism is
575 inconsistent with moderate to thick surface layers (> 20 nm) that display step function-like
576 jumps in cation concentrations. Nor is the diffusion model compatible with our measurements
577 that show no dependence of cation depletion depths on cation valence. Moreover, the fact that
578 the measured depths of depletion for Ca and Al are equal in our study is not consistent with
579 the leached layer model, because in general, framework elements like Al diffuse orders of
580 magnitude slower than interstitial cations (see e.g., Freer, 1981; Grove et al., 1984; Smith and
581 Brown, 1988; Brady and Cherniak, 2010). In addition, diffusion models cannot reproduce the
582 complexity of the chemical profiles measured for many of the minerals examined, e.g. garnet,
583 Fig. 2C; also K feldspar, Fig. 2D. And finally, our TEM and AFM observations suggest that
584 surface layers are permeable to the inward and outward fluxes of solution and product
585 species, respectively, and thus transport should not be diffusion limited. This effectively
586 means that alternative pathways, such as interconnected porosity, allow reactants ($H^+$ or
587 $H_3O^+$) to reach the pristine mineral surface much faster than by solid-state diffusion.
588 Moreover, our observations are in excellent agreement with those from Jordan et al. (1999),
589 who showed that despite the very rapid formation of an interfacial 'soft surface layer' on a
590 dissolving anorthite surface, the spreading of etch pits continued unimpeded beneath this
591 altered layer. Taken together, these results confirm that chemical reactions control the

592 destruction of the crystal lattice (i.e. reactions at pristine mineral interface, see Fig. 4), which
593 is at odds with the leached layer theory.
594 Diffusion profiles can be simulated that do show sharp concentration gradients,
595 provided that the altered layers are thin (<20nm; see Fig. 3C). In such cases, differentiating
596 the two mechanisms may be challenging. However, the mechanism proposed here explains
597 both thin or thick surface layers. In support of this are characteristic solid-state diffusion rates
598 that are many orders of magnitude too slow at room temperature to produce even thin
599 diffusion profiles, given the short time spans associated with laboratory-based non-
600 stoichiometric dissolution (1-10 days). This point is also borne out in a study by Hellmann et
601 al. (1992) where in situ AFM measurements showed the rapid formation (< 1 hour) of a
602 surface layer on albite feldspar at ambient conditions (compare to, e.g., Jordan et al., 1999).
603 The dissolution-reprecipitation mechanism we propose is, however, compatible with rapid
604 proton-cation exchange, as long as it is limited to the first monolayer of the mineral surface
605 (see e.g., Fenter et al., 2000).
606 *4.5. Interfacial dissolution-reprecipitaton mechanism*
607 We interpret the sharp chemical and structural interfaces measured in our study within
608 the framework of a coupled interfacial dissolution-reprecipitation mechanism, a mechanism
609 first hypothesized (but not proven at the time) for K-Na feldspar replacement by O'Neil and
610 Taylor (1967). Our study, for the first time, provides unambiguous evidence that unifies
611 laboratory and field chemical weathering of silicate minerals within the framework of this
612 concept. The key pieces of evidence that we present in support of this mechanism are:
613 a. nanometer-sharp chemical interfaces that are spatially coincident with the
614 structural interfaces (crystalline-amorphous boundary), and are present both on
615 laboratory and naturally weathered silicates
616 b. for any given mineral, the depths and gradients of cation depletion are equal for all
617 elements measured, irrespective of their valence and bonding nature (covalent:
618 framework cations vs. electrostatic: interstitial cations)
619 c. the short time durations (1-10 d) required to produce surface layers, even with
620 thicknesses of several hundreds of nm, are incompatible with extremely slow solid-state
621 volume diffusion rates at ambient temperatures

d. the precipitation of amorphous silica with high internal porosity- e.g. see Fig. 2B-ii, AFM images of the wollastonite (for details on porosity generation in secondary surface phases, refer to Pollok et al., 2011, see also review in Putnis, 2009)

The important processes of the coupled interfacial dissolution-reprecipitation mechanism, shown in Fig. 4, are:

a. dissolution occurs at a single reaction front in a thin fluid film in contact with the pristine mineral lattice; all constituent atoms are released to the fluid film at the same stoichiometric rate from the crystal lattice, irrespective of the pH, with no diffusion control and no preferential leaching

b. surface layers are formed by the contemporaneous, coupled precipitation of a distinct porous amorphous phase (Fig. 4)

c. precipitation of amorphous silica (i.e. acid to circum-neutral pH) occurs even when the bulk solution is undersaturated, which is perhaps attributable to the properties of thin fluid films in contact with mineral surfaces.

These three characteristics distinguish the dissolution-reprecipitation mechanism from current chemical weathering concepts, and specifically the leached layer model.

The interfacial dissolution-reprecipitation mechanism represents a significant step forward in understanding how chemical weathering works, for it allows for the first time the generalization that silica-rich surface layers can be treated thermodynamically as a single discrete phase. This is an obvious advantage for improved modeling of laboratory and natural chemical weathering reactions. Moreover, this mechanism is also compatible with published measurements that show an abrupt change in the composition of surface layers on altered feldspars from Si to Al-rich at circum-neutral to moderately basic pH conditions (Chou and Wollast, 1985; Nesbitt and Muir, 1988), a phenomenon difficult to explain with the leached layer theory. Related to this is the observation that significant (apparent) non-stoichiometric dissolution can even occur at basic pH (Hellmann, 1995), conditions not relevant for cation-proton exchange. And finally, dissolution-reprecipitation can better explain measurements that show continuous, apparent non-stoichiometric dissolution (e.g. wollastonite: this study; Weissbart and Rimstidt, 2000).

651 Interestingly, a recent Monte Carlo study also provides evidence in support of the
652 dissolution-reprecipitation mechanism. In their theoretical study of plagioclase dissolution
653 mechanisms, Zhang and Lüttge (2009) were able to reproduce the dependence of dissolution
654 rates on composition for the entire plagioclase series when dissolution was modeled via the
655 dissolution-reprecipitation mechanism, and not via thick leached layers.
656
657 *4.6. Properties of thin fluid films and precipitates*
658 A paradoxical aspect of our experiments and the interfacial dissolution-reprecipitation
659 mechanism is that silica-rich surface layers formed on mineral surfaces, even though the bulk
660 solutions were undersaturated with respect to possible secondary phases, in particular the
661 polymorphs of silica. In fact, the experiments took place at far-from-equilibrium conditions,
662 making the analysis of aqueous Si analytically challenging (i.e. low ppb range). Taking as an
663 example labradorite and wollastonite dissolution at acid pH conditions (pH 1 and pH 3,
664 respectively) and 25 °C, and recalling that both developed significant silica-rich surface layers
665 (≥ 400 nm), the highest recorded Si concentrations corresponded to respective solution
666 undersaturations (Gibbs free energy of reaction, $\Delta G$) of –4.6 and –6.3 kJ $mol^{-1}$ for quartz, and
667 –12.0 and –13.7 kJ $mol^{-1}$ for amorphous silica. It is interesting to note that the problematical
668 presence (from a thermodynamic point of view) of amorphous silica surface layers, formed at
669 conditions of silica undersaturation, has long been recognized (Iler, 1979; see also Casey et
670 al., 1993; Banfield et al., 1995). There are several possible, non-exclusive, explanations for
671 this phenomenon.
672 One possible reason is that the calculated solution saturation indices (free energy of
673 reaction, $\Delta G$) are possibly too low since they are based on pure (anhydrous) amorphous silica,
674 or other pure silica polymorphs (i.e. with respect to the thermodynamic data base of
675 geochemical codes, such as EQ3NR). The solubility of amorphous silica can be decreased by
676 several orders of magnitude by incorporation of foreign ions, especially Al, Ca, and Mg (Iler,
677 1979; Sposito, 1984). Minor amounts of these elements were always measured in the silica
678 layers formed after dissolution of the relevant minerals (Fig. 2C). In addition to foreign ions,
679 the solubility of amorphous silica has been shown to significantly decrease with increasing
680 degrees of hydration (Iler, 1979). Based on the significant concentration of H in the surface

681 layer formed on labradorite (see SIMS H profile, inset to Fig. 2A-i), it is likely that the degree
682 of hydration is generally elevated in surface layers.
683 Another possible reason is based on evidence that fluid molecules have a strong
684 tendency to order over distances of a few molecular layers from surfaces, due principally to
685 reduced orientational and translational entropy (Wang et al., 2006). The consequence of this is
686 that interfacial fluids have thermodynamic and physical properties that differ from those of
687 bulk fluids. Thus, molecular ordering of fluid molecules specifically affects such fluid
688 parameters as diffusion rates, viscosity, solute adsorption, the dielectric constant, and pH
689 (Fenter and Sturchio, 2004; Kerisit and Liu, 2009; see also review in Hochella and Banfield,
690 1995). These differences, in particular a decrease in the dielectric constant, have been
691 predicted to lead to enhanced solution saturation in thin fluid films (James and Healy, 1972;
692 Putnis et al., 1995), in excess of that due to the electrical double layer and surface adsorption
693 reactions. The nucleation process within the thin fluid film should theoretically not be
694 suppressed by diffusion, due to the extremely short distance between the reaction front and
695 the nucleation sites where eventually the secondary amorphous precipitate forms. We can
696 speculate that the thin fluid film is not thicker than 2-3 monolayers of (ordered) water, which
697 corresponds to approximately 7-10 Å; special fluid properties may even extend to 25 Å,
698 Kerisit and Liu, 2009. In addition, it is possible that the close proximity of the primary
699 mineral surface may serve to lower the nucleation energy barrier, enhancing the stability of
700 nuclei that form within the fluid film. Moreover, it has been experimentally observed that acid
701 pH conditions favor the polymerization of nano-colloidal silica particles that can eventually
702 lead to a highly stable silica gel (Iler, 1979). Nonetheless, there is still much uncertainty about
703 which combination of physical properties eventually allows a stable amorphous silica to
704 precipitate (despite bulk fluid undersaturation with respect to all silica polymorphs), and even
705 whether this is the result of equilibrium or non-equilibrium processes (e.g. Putnis, 1995).
706 While not possessing any long-range atomic order, it is possible that the short-range
707 order of the amorphous precipitated phase is controlled by the parent mineral structure, in
708 particular the degree of connectedness of the $SiO_4$ tetrahedra. Thus, the molecular structure of
709 an amorphous silica layer formed on olivine (composed of isolated $SiO_4$ tetrahedra) may be
710 different than the silica structure that forms on a feldspar (3-D framework of $SiO_4$ tetrahedra).

711 Going further, we can speculate that within a single family of minerals (e.g. the feldspar
712 plagioclase series), the differences in the parent structures may be transposed to the respective
713 surface layer structures.

714 The transfer of structural information from a dissolving crystalline mineral to an
715 amorphous silica precipitate was elegantly demonstrated by Müller et al. (1998). In that study,
716 the amorphous silica layer displayed a micro-lamellar structure identical to that of the parent
717 labradorite. In a similar fashion, carbonation reactions of wollastonite produced thick
718 amorphous silica rinds that perfectly replicated the underlying wollastonite structure (Daval et
719 al, 2009a, b). The generalized occurrence of an epitactic relationship between parent minerals
720 and product phases is one of the key characteristics of interface-coupled dissolution-
721 reprecipitation reactions (Putnis, 2009). Banfield et al. (1995) note that topotactic relations
722 among minerals are suggestive of transport of constituents across interfaces that are thin
723 enough to affect the properties of the fluid. While the mechanism for the transfer of structural
724 information via the fluid film is not fully understood (Putnis, 2002, 2009), it may be related to
725 the close spatial coupling of the reactions, which is in part related to the ordering of fluid
726 molecules controlled by the parent substrate.

727

728 *4.7. Growth of surface layers and their chemical composition*

729 The overall steady-state thicknesses of laboratory-created surface layers measured in
730 this study are quite variable. The properties of the fluid play an important role; the main
731 parameters that intervene are pH, bulk fluid saturation state, chemical composition, and
732 temperature. In addition to the fluid, the structure and chemistry of the parent mineral control
733 in large part the thickness of the surface layer (e.g. plagioclase feldspar series).

734 Even though the exact details on the processes generating surface layers are not
735 completely understood, these layers appear to be limited in thickness. The naturally weathered
736 K-feldspars examined in this study (Fig. 2D; exposure age ~ 14.7 ka) revealed surface layer
737 thicknesses on the order of 50 nm. For these samples, we differentiate the thin surface layers
738 (several tens of nm) from the several micron-thick over-layers containing phyllosilicates,
739 whose upper limit in thickness may not be controlled by chemical processes, but rather by
740 mechanical considerations. The exact interface separating the thin surface layer and the thick

741 over-layer is difficult to determine. In fact, referring to these layers as two separate entities
742 may not be correct, and could be considered subject to debate.
743 On the other hand, the thickness of the surface layer on the naturally weathered
744 serpentine (~150-200 nm, Fig. 2E) is unambiguous. The weathering exposure age for this
745 sample has not been determined, but is most likely far inferior to the granite (<< 14.7 ka),
746 based on the elevation, the deglaciation history of the Lac Robert area and surroundings (Le
747 Roux et al., 2009), and the fact that a present-day glacier is located just 1-2 km away. Another
748 example concerns K-feldspar grains retrieved from a Jurassic-age sandstone reservoir. These
749 feldspars show evidence of 10-50 nm-thick amorphous surface layers deficient in K and
750 enriched in Si (Zhu et al., 2006).
751 Considering that surface layers are primarily composed of amorphous silica, with minor
752 amounts of other elements originally present in the parent mineral, the overall thickness of the
753 layer at any point in time should be a function primarily of the Si budget: the time-integrated
754 amount of Si that precipitated in the thin film at the inner interface, less the amount of Si that
755 has been released to the bulk solution at the outer interface (refer to Fig. 4). Considering
756 weathering at far-from-equilibrium conditions (i.e. undersaturated bulk solutions), a steady-
757 state thickness can be achieved when the rate of Si precipitation within the thin fluid film
758 equals the rate of release of Si at the outer interface (i.e. the outer interface is not in
759 thermodynamic equilibrium with the bulk solution due to undersaturation).
760 Because the surface layer is permeable, the bulk fluid flow rate affects the thin fluid
761 film properties, and therefore the thickness of the surface layer. The fluid flow rate in a flow
762 reactor containing a mineral directly affects the degree of solution saturation of the bulk fluid
763 (i.e. the slower the flow, the higher the fluid residence time, which induces a higher degree of
764 bulk solution saturation). As an example, the wollastonite alteration experiments were
765 conducted at several different flow rates, with the slower flow rates producing significantly
766 thicker silica surface layers. These observations can be interpreted in terms of a retardation of
767 the dissolution rate at the external silica-fluid interface, or an increase in the rate of silica
768 precipitation at the internal interface, or perhaps even both (see also Daval et al., 2011). The
769 effect of fluid flow on surface layer thicknesses has also been observed for orthoclase
770 feldspar. Using X-ray reflectivity, Teng and co-workers (2001) observed the formation of a

771 very thin silica gel-like surface coating at acidic conditions under slow fluid flow-rate
772 conditions, whereas at high fluid flow-rate conditions, no coating was observed. Taken
773 together, these observations are consistent with the dissolution-reprecipitation mechanism,
774 because they demonstrate a positive feedback between solution saturation and surface layer
775 thickness. On the other hand, considering the leached layer mechanism, one would predict
776 that decreasing the flow fluid flow-rate would increase the build up of product ions at the
777 external interface and decrease the diffusion gradient, thereby leading to thinner leached
778 layers. This is contrary to the results discussed above.

779 All of the laboratory minerals altered at acid pH displayed surface layers enriched in Si
780 compared to the parent mineral (see Fig. 2). This has also been evidenced in other studies of
781 acid-pH, laboratory-altered silicates (e.g. Mogk and Locke, 1988; Schweda et al., 1997;
782 Nesbitt and Skinner, 2001; Kameda et al., 2009). In the present study, the naturally weathered
783 serpentine also showed Si enrichment in the surface layer, but on the other hand, the K-
784 feldspar from the granite showed essentially no change in Si concentration. Other studies in
785 the literature reporting on natural alteration of silicate minerals in contact with acid pH
786 solutions also show Si enrichment (e.g. Kawano and Tomita, 2001).

787 We interpret surface layers enriched in Si to be consistent with the dissolution-
788 reprecipitation model. In this study, the normalized concentration of Si in representative
789 parent minerals ranged from 20 to 25 wt. % (i.e. pyrope garnet = 19.6, wollastonite = 24.2,
790 and labradorite feldspar = 25.0 wt %). These Si concentrations can be compared with the
791 theoretical concentration of Si in a precipitated $SiO_2$ surface layer, which equals 46 wt. %
792 (slightly less if hydration is factored in). Therefore, if the surface layer represents a discrete
793 precipitated phase, then one would expect a jump in Si concentration at the inner interface
794 (i.e. the mineral-amorphous layer boundary), which indeed is what we measured (see Figs.
795 2A, B, C, E). The magnitude of the concentration jumps will be less if it is assumed (from BF
796 and DF TEM images) that the surface layers are lower in density.

797 Moreover, there is no a priori reason why Si enrichment would be expected for silica-
798 rich surface altered layers formed by preferential cation loss from the mineral structure (i.e.
799 leached layers). The only feasible alternative for a silica-rich relict layer to display an increase
800 in Si concentration (i.e. Si atoms per unit volume) compared to the parent mineral is through

801 significant structural reorganization, by processes such as condensation and densification. As
802 an example, in their laboratory investigation of chlorite alteration (Kameda et al., 2009), the
803 surface altered region is characterized by elevated Si levels (90-95 avg. EDX counts in silica
804 layer vs. 65 avg. counts in pristine chlorite). The authors attribute this enrichment to
805 hydrolysis-recondensation reactions. While this explanation is plausible, the BF TEM images
806 appear to show that the altered zone is uniformly less electron dense than the chlorite, with no
807 dark, electron dense zones present (as might be expected for layer densification or collapse;
808 e.g. compare to dark banding attributed to densification of altered gel layer on a borosilicate
809 glass, Cailleteau et al., 2008). To resolve this question, one possibility would be to simulate
810 BF TEM images of chlorite in contact with Si layers having variable densities.
811 With respect to the silica layers observed in our samples, we see no obvious evidence
812 for densification. The aqueous solution data do not show any significant drop in release rates
813 of cations with time, which would be indicative of densification, in particular if the silica
814 layer were to become passivating. The TEM images also do not show any obvious signs of
815 densification, even though we note the presence of some slightly darker bands in some of the
816 HRTEM images (see, e.g. Fig. 2A-ii, C, D). The origin of these darker bands merits a more
817 detailed investigation. In conclusion, even though we cannot completely rule out densification
818 processes in surface layers, at present we do not ascribe the measured Si enrichments
819 measured in our study to such processes.
820
821 *4.8. Internal porosity of surface layers*
822 A key tenet of the interfacial dissolution-reprecipitation mechanism is that the
823 precipitate does not act as a protective surface layer, such that the transport of aqueous
824 chemical reactants and products between the crystalline reaction front and bulk fluid (inner
825 and outer interfaces, respectively, Fig. 4) is not diffusion controlled (Putnis, 2009). The
826 generation of porosity in secondary crystalline phases is in fact generally observed for mineral
827 replacement reactions (Harlov et al., 2005; Putnis et al., 2007; see also examples in Putnis,
828 2002, 2009). Development of significant internal porosity within amorphous surface (altered)
829 layers has also been reported (e.g. Casey et al., 1989, 1993; Weissbart and Rimstidt, 2000).

In the present study, the molar volume changes associated with the precipitation of amorphous silica are negative ($V_{\text{amor silica}} / V_{\text{mineral}} < 1$). The Pilling-Bedworth rule predicts the generation of internal porosity within a precipitate when the molar volume ratio of product to parent phase is less than one (see, e.g. Velbel, 1993). More recent work points out that the generation of porosity in the secondary phase depends on both the molar volume change and the difference in relative solubilities of the parent and product phases (Putnis, 2009; Pollok et al., 2011). In the present study, the constant, steady-state cation release rates measured during each mineral alteration experiment are consistent with permeable, non-passivating surface layers (i.e. weathering kinetics were unaffected). Furthermore, the sharp nanoscale chemical gradients measured by EFTEM (Fig. 2) at the mineral-surface layer interfaces, with respect to both laboratory and natural weathering, also indicate that the reactions were not kinetically hindered by solid-state volume diffusion.

Direct evidence for elevated secondary porosity comes from observations of the 3-D surface structures on two of the laboratory-altered minerals, labradorite and wollastonite. Figure 2B-ii shows a tapping mode AFM image of an altered wollastonite surface, composed primarily of amorphous hydrated silica, which is characterized by botryoidal morphology and significant near-surface porosity, with heterogeneous pore spaces ranging from a few tens of nm up to a hundred nm in diameter. Recent molecular dynamics simulations (Kerisit and Liu, 2009) show that self-diffusion coefficients of water and electrolyte ions are not affected by pore size until a critical value of 5 nm is reached; in pore spaces < 5nm in diameter there is a notable decrease with respect to bulk fluid values. The near-surface pores imaged here are largely superior to this critical diameter. In addition, whether the formation of a high porosity, botryoidal surface by the interdiffusion-leached layer mechanism is plausible is highly questionable. We therefore argue that the AFM images support the premise that the surface layers produced in the laboratory experiments did not impede the inward and outward flux of aqueous species.

Even though we have argued that the surface silica layers studied here were not passivating, this may not always be true. A case in point is the study by Daval et al. (2011) on coupled weathering-carbonation reactions on olivine. According to their study, the silica layers (20-40 nm) that originally formed on the olivine surface by dissolution-reprecipitation

860 became passivating with increasing reaction progress, due to an internal densification process.
861 Their argument is based on the measured reaction rates of olivine that showed evidence for
862 significant retardation, and the fact that the Mg chemical gradients (measured by STEM-
863 EDX) at the internal interface were slightly sigmoidal. Perhaps this particular behavior of
864 olivine was specifically due to alteration in aqueous solutions with high $pCO_2$. A convincing
865 example of densification and pore closure in surface (altered) layers formed on borosilicate
866 glasses can be found in the study of Cailleteau et al. (2008).

867 In general, surface precipitates that form during weathering should be considered to be
868 dynamic and subject to structural modification. In his review of mineral replacement
869 reactions, Putnis (2009) states that as long as the porous precipitate is in contact with an
870 aqueous solution, its microstructure will continue to evolve with time via dissolution-
871 reprecipitation reactions (see, e.g. porosity coarsening, Putnis et al., 2005). The in situ
872 nucleation and crystallization of secondary phases, in particular clay minerals, is also
873 commonly observed (e.g. present study, feldspar- see text and Fig. 2D). Silicates reacted at
874 high $pCO_2$ can result in silica layers that contain in situ precipitated carbonates (Daval et al.,
875 2009b) that may render them passivating.

876

877 **5. Conclusions and Broader Implications**

878 One of the most important results of this study is that chemical weathering reactions
879 which lead to the generalized occurrence of amorphous surface layers are controlled by
880 interfacial dissolution-reprecipitation. This finding considerably extends the original research
881 on nanoscale alteration of feldspar surfaces by Hellmann et al., 2003. The dissolution-
882 reprecipitation mechanism allows us for the first time to unify simple weathering reactions in
883 the laboratory with complex natural weathering that occurs in the field. We can now take our
884 reasoning a step further and combine our results with recent studies on mineral-mineral
885 replacement reactions, which can be thought of as another type of chemical weathering
886 process. The pioneering research of Goldsmith and Laves (1954), O'Neil and Taylor (1967),
887 and Mérigoux (1968) effectively established the theoretical foundation for a large number of
888 recent analytical studies on mineral replacement, encompassing both laboratory and natural
889 conditions, and at ambient as well as at elevated temperatures. These studies have all

advocated an interfacial dissolution-reprecipitation mechanism (e.g. Fiebig and Hoefs, 2002; Labotka et al., 2004; Putnis and Mezger, 2004; Putnis et al., 2005; Harlov et al., 2002, 2005; Harlov and Förster, 2003; Geisler et al., 2007; Putnis and Putnis, 2007; Hövelmann et al., 2010; see also extensive reviews in Putnis, 2002, 2009, and references therein). Even though the intrinsic mechanism is the same, the major difference between these two types of weathering processes is that in the former the surface layer is an amorphous phase, whereas in the latter the secondary phase is crystalline. When all of these studies are considered together, it can be argued that the interfacial dissolution-reprecipitation mechanism is a universal phenomenon that controls all mineral-water interactions (Putnis and Putnis, 2007).

Because our results concur with the idea of a universal mineral-water alteration mechanism, we therefore redefine the continuum model of weathering described by Hochella and Banfield (1995). In their model, proton-cation exchange characterizes the laboratory end-member (i.e. leached layers, which in some cases can also occur in nature), whereas the natural weathering end-member is characterized by mineral replacement occurring by direct (i.e. solid-state) structural transformation.

Instead, we propose a continuum model that is based on interfacial dissolution-reprecipitation as the principal mechanism of chemical weathering. In this model no distinction is made between laboratory and natural weathering, but rather, the nature of the secondary phase is used to define the two end-members of the continuum. One of the poles defines weathering reactions characterized by the precipitation of amorphous surface phases; the other pole is defined by weathering reactions leading to mineral-mineral replacement reactions. Mineral weathering characterized by amorphous phases that contain in situ-nucleated and crystallized secondary phases (i.e. clays) can be considered as lying between the two poles (see Fig. 4). In the present study, most of the minerals studied fall into the domain characterized by amorphous surface precipitates. The weathering of K-feldspar (Fig. 2D) is an example of weathering where the products are both amorphous and crystalline. In this case, we assume that the amorphous silica contained the precursor nucleii that permitted the in situ crystallization of the phyllosilicates that we observed.

The differences in the physical and chemical conditions associated with specific weathering environments that lead to either amorphous surface layers or mineral replacement

920 are not precisely known. Given that in the present study amorphous silica layers formed
921 during laboratory alteration in very dilute aqueous solutions, whereas mineral replacement
922 reactions commonly occur in the presence of solutions enriched in certain chemical species
923 (e.g. albite replaced by K-feldspar in solutions enriched in KCl, Labotka et al., 2004), it is
924 possible that the reprecipitation reactions corresponding to the two poles are controlled by the
925 chemical saturation state and the chemical composition of the bulk fluids associated with the
926 weathering process; temperature, and to a lesser degree, pressure, may play subsidiary roles.
927 These parameters have a direct influence on the physical and chemical properties of the
928 interfacial thin fluid film (Fig. 4). Kinetic considerations may also play an important role in
929 the reprecipitation process.

930 The generalized presence of precipitated silica layers has potential significance with
931 respect to the global C cycle and the total amount of $CO_2$ consumed during weathering, in
932 particular for reactive ultramafic rocks (e.g. ophiolites) or industrial $CO_2$ carbonation-
933 sequestration processes. Even though clays and other neo-formed minerals can affect the $CO_2$
934 budget, our results show that precipitated surface silica layers retain minor amounts of
935 divalent metal cations. Their presence potentially reduces both carbonate formation and $CO_2$
936 consumption. Secondary carbonate precipitates, thermodynamically favored during
937 weathering in the presence of high $HCO_3^-$ concentrations (i.e. high $pCO_{2\,aq}$), may even
938 kinetically hinder chemical weathering due to pore clogging within amorphous silica layers
939 (Daval et al., 2009a, b), thereby further reducing $CO_2$ consumption.

940 Our results show the potential of the approach we have used for studying fluid-mineral
941 and fluid-solid interactions, with potentially diverse applications in the geosciences and in
942 other fields, such as near- and far-field fluid-solid interactions associated with radioactive
943 waste repositories (e.g. mechanism of actinide incorporation into surface layers formed either
944 on glasses or minerals), biomineralization, dental and medical sciences (e.g., periodontal
945 decay, e.g. Elliot et al., 2005; interaction of bone with biofluids), electrochemistry (e.g.
946 corrosion reactions at metal-solution interfaces), dissolution and reactivity of natural and
947 man-made nanomaterials, and tribology (e.g. seismogenic fault behavior related to diminution
948 of the friction coefficient due to fluid-mineral interactions, e.g. Moore and Rymer, 2007,
949 and/or the presence of silica gel layers on fault surfaces). Given the current interest in finding

water on Mars, we propose that the potential presence of hydrous, silica-rich surface layers on exposed Martian plagioclases could serve as evidence for chemical weathering reactions in the former presence of free water.

It is interesting to speculate further on the coupled interfacial dissolution-reprecipitation reaction that applies to silicate mineral-fluid reactions, for it may in fact be a more universal phenomenon. Recent experimental findings concerning melt migration through olivine at mantle conditions (Schiano et al., 2006) overturn current thinking by providing strong evidence that this process is not diffusion controlled, but rather occurs via a sharp crystal-melt reaction front whose advance is controlled by partial melting (detachment, analogous to dissolution), followed by crystallization (attachment, analogous to reprecipitation).

## ACKNOWLEDGMENTS

This work was supported by INSU 3F, INSU-EC2CO, INSU-SYSTER, METSA (CEA-CNRS), and ISTerre grants to R.H.; the French Basic Technological Research (RTB) program to J.-P.B.; we thank CLYM for access to the Jeol 2010F TEM. We also acknowledge G. Brocard for the $^{10}$Be exposure age of the glacial erratic boulder, and useful discussions on multi-component diffusion with J. Brady. Constructive comments from 2 anonymous reviewers and the editor were appreciated.

## REFERENCES CITED

Arnold, G.W., Westrich, H.R., Casey, W.H., 1992. Application of ion beam analysis (RBS and ERD) to the surface chemistry study of leached minerals. Nuclear Instruments and Methods in Physics Research Section B, B64, 542-546.

Bandstra, J.Z., Buss, H.L., Campen, R.K., Liermann, L.J., Moore, J., Hausrath, E.M., Navarre-Sitchler, A.K., Jang, J.-H., Brantley S.L., 2008. Appendix: Compilation of mineral dissolution rates. In: Brantley, S.L., Kubicki, J.D., White, A.F. (Eds.), Kinetics of Water-Rock Interaction. Springer, New York, 737-823.

Banfield, J.F., Eggleton, R.A., 1990. Analytical transmission electron microscope studies of plagioclase, muscovite, and K-feldspar weathering. Clays and Clay Minerals 38, 77-89.

Banfield, J.F., Ferruzzi, G.G., Casey, W.H., Westrich, H.R., 1995. HRTEM study comparing naturally and experimentally weathered pyroxenoids. Geochimica et Cosmochimica Acta 59, 19-31.

Barker, W.W., Welch, S.A., Chu, S., Banfield, J.F., 1998, Experimental observations of the effects of bacteria on aluminosilicate weathering. American Mineralogist 83, 1551-1563.

986 Berner, R.A., Holdren, G.R. Jr., 1977. Mechanism of feldspar weathering: some observational
987 evidence. Geology 5, 369-372.
988 Berner, R.A., Holdren, G.R. Jr., 1979, Mechanism of feldspar weathering- II. Observations of
989 feldspars from soils. Geochimica et Cosmochimica Acta 43, 1173-1186.
990 Berner, E.K., Berner, R.A., Moulton, K.L., 2003, Plants and mineral weathering: Present and
991 Past, In: Drever, J.I., (Ed.), Surface and Ground Water, Weathering, and Soils.
992 Elsevier-Pergammon, Oxford, pp. 169-188.
993 Blum, A.E., Stillings, L.L., 1995. Feldspar dissolution kinetics. In: White, A.F. and Brantley,
994 S.L. (Eds.), Chemical Weathering Rates of Silicate Minerals. Reviews in Mineralogy.
995 Mineralogical Society of America, Washington, D.C., pp. 291-351.
996 Bonneville, S., Smits, M.M., Brown, A., Harrington, J., Leake, J.R., Brydson, R., Benning,
997 L.G., 2009, Plant-driven fungal weathering: Early stages of mineral alteration at the
998 nanometer scale. Geology 37, 615-618.
999 Brady, J.B., 2010. Diffusion in minerals: An overview of published experimental diffusion
1000 data. In: Zhang Y. and Cherniak, D.J. (Eds.), Diffusion in Minerals and Melts.
1001 Reviews in Mineralogy & Geochemistry. Mineralogical Society of America,
1002 Washington, D.C., pp. 899-920.
1003 Brantley, S.L., 2003, Reaction kinetics of primary rock-forming minerals under ambient
1004 conditions. In: Drever, J.I. (Ed.), Surface and Ground Water, Weathering, and Soils.
1005 Elsevier-Pergammon, Oxford, pp. 73-117.
1006 Brantley, S.L., 2008. Kinetics of Mineral Dissolution. In: Brantley, S.L., Kubicki, J.D.,
1007 White, A.F. (Eds.), Kinetics of Water-Rock Interaction. Springer, New York, pp. 151-
1008 210.
1009 Bunker, B.C., Tallant, D.R., Headley, T.J., Turner, G.L., Kirkpatrick, R.J., 1988. The
1010 structure of leached sodium silicate glass. Physics and Chemistry of Glasses 29, 106-
1011 120.
1012 Cailleteau, C., Angeli, F., Devreux, F., Gin, S., Jestin, J., Jollivet, P., Spallaet, O., 2008.
1013 Insight into silicate-glass corrosion mechanisms. Nature Materials 7, 978-983.
1014 Casey, W.H., Bunker, B., 1990. Leaching of mineral and glass surfaces during dissolution. In:
1015 Hochella, M.F. Jr., White, A.F. (Eds.), Mineral-Water Interface Geochemistry.
1016 Reviews in Mineralogy. Mineralogical Society of America, Washington, D.C., pp.
1017 397-426.
1018 Casey, W.H., Westrich, H.R., Arnold, G.W., 1988. Surface chemistry of labradorite feldspar
1019 reacted with aqueous solutions at pH = 2, 3, and 12. Geochimica et Cosmochimica
1020 Acta 52, 2795-2807.
1021 Casey, W.H., Westrich, H.R., Massis, T., Banfield, J.F., Arnold, G.W., 1989. The surface of
1022 labradorite feldspar after acid hydrolysis. Chemical Geology 78, 205-218.
1023 Casey, W.H., Westrich, H.R., Banfield, J.F., Ferruzzi, G., Arnold, G.W., 1993. Leaching and
1024 reconstruction at the surfaces of dissolving chain-silicate minerals. Nature 366, 253-
1025 255.
1026 Chardon, E.S., Livens, F.R., Vaughan, D.J., 2006. Reactions of feldspar surfaces with
1027 aqueous solutions. Earth-Science Reviews 78, 1-26.
1028 Chou, L., Wollast, R., 1985. Steady-state kinetics and dissolution mechanisms of albite.
1029 American Journal of Science 285, 963-993.
1030 Daval, D., Martinez, I., Corvisier, J., Findling, N., Goffé, B., Guyot, F., 2009a. Carbonation
1031 of Ca-bearing silicates, the case of wollastonite: Experimental investigations and
1032 kinetic modelling. Chemical Geology 265**,** 63–78.
1033 Daval, D., Martinez, I., Guigner, J.-M., Hellmann, R., Corvisier, J., Findling, N., Dominici,
1034 C., Goffé, B., Guyot, F., 2009b. Mechanism of wollastonite carbonation deduced from
1035 micro- to nanometer length scale observations. American Mineralogist 94, 1707-1726.
1036 Daval, D., Sissmann, O., Menguy, N., Saldi, G.D., Guyot, F., Martinez, I., Corvisier, J.,
1037 Garcia, B., Machouk, I., Knauss, K.G., Hellmann, R., 2011, Influence of amorphous

1038 silica layer formation on the dissolution rate of olivine at 90 °C and elevated $pCO_2$.
1039 Chemical Geology 284, 193-209.
1040 Dixon, J.C., Thorn, C.E., Darmody, R.G., Campbell, S.W., 2002. Weathering rinds and rock
1041 coatings from an Arctic alpine environment, northern Scandinavia. Geological Society
1042 of America Bulletin 114, 226-238.
1043 Drever, J.I., ed., 2003, Surface and Ground Water, Weathering, and Soils. Elsevier,
1044 Amsterdam, 626 p.
1045 Elliott, J.C., Bollet-Quivogne, F.R.G., Anderson, P., Dowker, S.E.P., Wilson, R.M., Davis, G.
1046 R., 2005. Acidic demineralization of apatites studied by scanning X-ray
1047 microradiography and microtomography. Mineralogical Magazine 69, 643-652.
1048 Fenter, P., Sturchio, N.C., 2004. Mineral-water interfacial structures revealed by synchrotron
1049 X-ray scattering. Progress in Surface Science **77**, 171-258.
1050 Fenter, P., Teng, H., Geissbühler, P., Hanchar, J.M., Nagy, K.L., Sturchio, N.C., 2000.
1051 Atomic-scale structure of the orthoclase (001)-water interface measured with high-
1052 resolution X-ray reflectivity. Geochimica et Cosmochimica Acta 64, 3663-3673.
1053 Fiebig, J., Hoefs, J., 2002. Hydrothermal alteration of biotite and plagioclase as inferred from
1054 intragranular oxygen isotope- and cation-distribution patterns. European Journal of
1055 Mineralogy 14, 49-60.
1056 Freer, R., 1981. Diffusion in silicate minerals and glasses: A data digest and guide to the
1057 literature. Contributions to Mineralogy and Petrology 76, 440-454.
1058 Garrels, R.M., Howard, P., 1957. Reactions of feldspar and mica with water at low
1059 temperature and pressure. Clays and Clay Minerals 6, 68-88.
1060 Geisler, T., Schaltegger, U., Tomaschek, F., 2007. Re-equilibration of zircon in aqueous
1061 fluids and melts. Elements 3, 43-50.
1062 Geisler, T., Janssen, A., Scheiter, D., Stephan, T., Berndt, J., Putnis, A., 2010. Aqueous
1063 corrosion of borosilicate glass under acidic conditions: A new corrosion mechanism.
1064 Journal of Non-Crystalline Solids 356, 1458-1465.
1065 Goldsmith, J.R., Laves, F., 1954. The microcline-sanidine stability relations. Geochimica et
1066 Cosmochimica Acta 5, 1-19.
1067 Grove, T.L., Baker, M.B., Kinzler, R.J., 1984. Coupled CaAl-NaSi diffusion in plagioclase
1068 feldspar: Experiments and applications to cooling rate speedometry. Geochimica et
1069 Cosmochimica Acta 48, 2113-2121.
1070 Harlov, D.E., Förster, H.-J., 2003. Fluid-induced nucleation of (Y + REE)-phosphate minerals
1071 within apatite: Nature and experiment. Part II. Fluorapatite. American Mineralogist
1072 88, 1209-1229.
1073 Harlov, D.E., Förster, H.-J., Nijland, T.G., 2002. Fluid-induced nucleation of (Y + REE)-
1074 phosphate minerals within apatite: Nature and experiment. Part I. Chlorapatite.
1075 American Mineralogist 87, 245–261.
1076 Harlov, D.E., Wirth, R., Förster, H.-J., 2005. An experimental study of dissolution-
1077 reprecipitation in fluorapatite: fluid infiltration and the formation of monazite.
1078 Contributions to Mineralogy and Petrology 150, 268-286.
1079 Hellmann, R., 1994. The albite-water system Part I. The kinetics of dissolution as a function
1080 of pH at 100, 200 and 300°C, Geochimica et Cosmochimica Acta 58, 595-611.
1081 Hellmann, R., 1995, The albite-water system Part II. The time-evolution of the stoichiometry
1082 of dissolution as a function of pH at 100, 200 and 300°C. Geochimica et
1083 Cosmochimica Acta 59, 1669-1697.
1084 Hellmann, R., 1997. The albite-water system Part IV. Diffusion modeling of leached and
1085 hydrogen-enriched layers. Geochimica et Cosmochimica Acta 61, 1595-1611.
1086 Hellmann, R., Drake, B., Kjoller, K., 1992. Using atomic force microscopy to study the
1087 structure, topography and dissolution of albite surfaces. In: Kharaka, Y.K., Maest,
1088 A.S. (Eds.), Water-Rock Interaction 7. A.A. Balkema, Rotterdam, pp. 149-152.

1089 Hellmann, R., Dran, J.-C., Della Mea, G., 1997. The albite-water system Part III.
1090 Characterization of leached and hydrogen-enriched layers formed at 300°C using
1091 MeV ion beam techniques. Geochimica et Cosmochimica Acta 61, 1575-1594.
1092 Hellmann, R., Penisson, J.M., Hervig, R.L., Thomassin, J.H., Abrioux, M.F., 2003. An
1093 EFTEM/HRTEM high-resolution study of the near surface of labradorite feldspar
1094 altered at acid pH: evidence for interfacial dissolution-reprecipitation. Physics and
1095 Chemistry of Minerals 30, 192-197.
1096 Hellmann, R., Penisson, J.-M., Hervig, R.L., Thomassin, J.-H., Abrioux, M.F., 2004.
1097 Chemical alteration of feldspar: a comparative study using SIMS and
1098 HRTEM/EFTEM. In: Wanty, R.B., Seal, R.R. II (Eds.), Water Rock Interaction. A.A.
1099 Balkema, Rotterdam, pp. 753-756.
1100 Hochella, M.F. Jr., Banfield, J.F., 1995. Chemical weathering of silicates in nature: A
1101 microscopic perspective with theoretical considerations. In: Ribbe, P.H. (Ed.),
1102 Chemical Weathering Rates of Silicate Minerals. Reviews in Mineralogy.
1103 Mineralogical Society of America, Washington, D.C., pp. 353-406.
1104 Hofer, F., Grogger, W., Kothleitner, G., Warbichler, P., 1997. Quantitative analysis of
1105 EFTEM elemental distribution images. Ultramicroscopy 67, 83-103.
1106 Hövelmann, J., Putnis, A., Geisler, T., Schmidt, B.C., Golla-Schinder, U., 2010. The
1107 replacement of plagioclase feldspars by albite: observations from hydrothermal
1108 experiments. Contributions to Mineralogy and Petrology 159, 43-59.
1109 Iler, R. K., 1979, The Chemistry of Silica. John Wiley & Sons, New York.
1110 Inskeep, W.P., Nater, E.A., Bloom, P.R., Vandervoort, D.S., Erich, M.S., 1991.
1111 Characterization of laboratory weathered labradorite surfaces using X-ray
1112 photoelectron spectroscopy and transmission electron microscopy. Geochimica et
1113 Cosmochimica Acta 55, 787-800.
1114 James, R.O., Healy, T.W., 1972. Adsorption of hydrolysable metal ions at the oxide-water
1115 interface. II. Charge reversal of $SiO_2$ and $TiO_2$ colloids by adsorbed Co(II), La(III),
1116 and Th(IV) as model systems. Journal of Colloid Interface Science 40, 53-64.
1117 Jordan, G., Higgins, S.R., Eggleston, C.M., Swapp, S.M., Janney, D.E., Knauss, K.G., 1999.
1118 Acidic dissolution of plagioclase: In-situ observations by hydrothermal atomic force
1119 microscopy. Geochimica et Cosmochimica Acta 63, 3183-3191.
1120 Kameda, J., Sugimori, H., Murakami, T., 2009. Modification of the crystal structure of
1121 chlorite during early stages of its dissolution. Physics and Chemistry of Minerals 36,
1122 537-544.
1123 Kawano, M., Tomita, K., 2001, TEM-EDX study of weathered layers on the surface of
1124 volcanic glass, bytownite, and hypersthene in volcanic ash from Sakurajima volcano,
1125 Japan. American Mineralogist 86, 284-292.
1126 Kerisit, S., Liu, C., 2009, Molecular simulations of water and ion diffusion in nanosized
1127 mineral fractures. Environmental Science and Technology 43, 777-782.
1128 King, H.E., Plümper, O., Geisler, T., Putnis, A., 2011. Experimental investigations into the
1129 silicification of olivine: Implications for the reaction mechanism and acid
1130 neutralization. American Mineralogist, 96, 1503-1511.
1131 Labotka, T.C., Cole, D.R., Fayek, M., Riciputi, L.R., Stadermann, F.J., 2004, Coupled cation
1132 and oxygen-isotope exchange between alkali feldspar and aqueous chloride solution.
1133 American Mineralogist 89, 1822-1825.
1134 Lanford, W.A., Davis, K., Lamarche, P., Laursen, T., Groleau, R., 1979. Hydration of soda-
1135 lime glass. Journal of Non-Crystalline Solids 33, 249-266.
1136 Le Roux, O., Schwartz, S., Gamond, J.-F., Jongmans, D., Bourles, D., Braucher, R.,
1137 Mahaney, W., Carcaillet, J., Leanni, L., 2009. CRE dating on the head scarp of a
1138 major landslide (Séchilienne, French Alps), age constraints on Holocene kinematics.
1139 Earth and Planetary Science Letters 280, 236-245.

1140 Lee, M.R., Parsons, I., 1998. Microtextural controls of diagenetic alteration of detrital alkali
1141 feldspars: a case study of the Shap conglomerate (Lower Carboniferous), Northwest
1142 England. Journal of Sedimentary Research 68, 198-211.
1143 Lee, M.R., Brown, D.J., Smith, C.L., Hodson, M.E., MacKenzie, M., Hellmann, R., 2007.
1144 Characterization of mineral surfaces using FIB and TEM: A case study of naturally
1145 weathered alkali feldspars. American Mineralogist 92, 1383-1394.
1146 Lee, M.R., Hodson, M.E., Brown, D.J., MacKenzie, M., Smith, C.L., 2008. The composition
1147 and crystallinity of the near-surface regions of weathered alkali feldspars. Geochimica
1148 et Cosmochimica Acta 72, 4962-4975.
1149 Luce, R.W., Bartlett, R.W., Parks, G.A., 1972. Dissolution kinetics of magnesium silicates.
1150 Geochimica et Cosmochimica Acta 36, 35-50.
1151 Maher, K., Steefel, C.I., White, A.F., Stonestrom, D.A., 2009, The role of reaction affinity
1152 and secondary minerals in regulating chemical weathering rates at the Santa Cruz Soil
1153 Chronosequence, California. Geochimica et Cosmochimica Acta 73, 2804-2831.
1154 Mérigoux, H., 1968. Étude de la mobilité de l'oxygène dans les feldspaths alcalins. Bulletin de
1155 la Societé française de Minéralogie et Cristallographie 91, 51-64.
1156 Mogk, D.W., 1990. Application of Auger electron spectroscopy to studies of chemical
1157 weathering. Reviews of Geophysics 28, 337-356.
1158 Mogk, D.W., Locke, W.W. III, 1988. Application of Auger Electron Spectroscopy (AES) to
1159 naturally weathered hornblende. Geochimica et Cosmochimica Acta 52, 2537-2542.
1160 Moore, D.E., Rymer, M.J., 2007, Talc-bearing serpentinite and the creeping section of the San
1161 Andreas fault. Nature 448, 795-797.
1162 Müller, W.F., Pentinghaus, H., Kronimus, B., 1998. Lamellar microstructure of amorphous
1163 silica from leached labradorite feldspar. Neues Jahrbuch für Mineralogische
1164 Abhandlungen 172, 145-159.
1165 Muir, I.J., Bancroft, G.M., Nesbitt, H.W., 1989. Characteristics of altered labradorite surfaces
1166 by SIMS and XPS. Geochimica et Cosmochimica Acta 53, 1235-1241.
1167 Muir, I.J., Bancroft, G.M., Shotyk, W., Nesbitt, H.W., 1990. A SIMS and XPS study of
1168 dissolving plagioclase. Geochimica et Cosmochimica Acta 54, 2247-2256.
1169 Nash, V.E., Marshall, C.E., 1956. The surface reactions of silicate minerals Part I. The
1170 reactions of feldspar surfaces with acidic solutions. Research Bulletin, College of
1171 Agriculture, University of Missouri 613, 1-36.
1172 Nesbitt, H.W., Muir, I.J., 1988. SIMS depth profiles of weathered plagioclase, and processes
1173 affecting dissolved Al and Si in some acidic soil conditions. Nature 334, 336-338.
1174 Nesbitt, H.W., Skinner, W.M., 2001. Early development of Al, Ca, and Na compositional
1175 gradients in labradorite leached in pH 2 HCl solutions. Geochimica et Cosmochimica
1176 Acta 65, 715-727.
1177 Nugent, M.A., Brantley, S.L., Pantano, C.G., Maurice, P.A., 1998. The influence of natural
1178 mineral coatings on feldspar weathering. Nature 395, 588-591.
1179 Ohlin, C.A., Villa, E.M., Rustad, J.R., Casey, W.H., 2010. Dissolution of insulating oxide
1180 materials at the molecular scale. Nature Materials 9, 11-19.
1181 O'Neil, J.R., Taylor, H.P.J., 1967. The oxygen isotope and cation exchange chemistry of
1182 feldspars. American Mineralogist 52, 1414-1437.
1183 Paces, T., 1973. Steady-state kinetics and equilibrium between ground water and granitic
1184 rock. Geochimica et Cosmochimica Acta 37, 2641-2663.
1185 Parsons, I., 1978. Feldspars and fluids in cooling plutons. Mineralogical Magazine 42, 1-17.
1186 Pederson, L.R., Baer, D.R., McVay, G.L., Engelhard, M.H., 1986. Reaction of soda-lime
1187 silicate glass in isotopically labelled water. Journal of Non-Crystalline Solids 86, 369-
1188 380.
1189 Petit, J.C., Dran, J.C., Paccagnella, A., Della Mea, G., 1989. Structural dependence of
1190 crystalline silicate hydration during aqueous dissolution. Earth and Planetary Science
1191 Letters 93, 292-298.

1192 Petit, J.C., Dran, J.C., Della Mea, G., 1990. Energetic ion beam analysis in the Earth sciences.
1193 Nature 344, 621-626.
1194 Perez, R.J., Boles, J.R., 2005. An empirically derived kinetic model for albitization of detrital
1195 plagioclase. American Journal of Science 305, 312-343.
1196 Pollok, K., Putnis, C.V., Putnis, A., 2011. Mineral replacement reactions in solid solution-
1197 aqueous solution systems: volume changes, reaction paths and end-points using the
1198 example of model salt systems. American Journal of Science, 311, 211-236.
1199 Putnis, A., 2002. Mineral replacement reactions: from macroscopic observations to
1200 microscopic mechanisms. Mineralogical Magazine 66, 689-708.
1201 Putnis, A., 2009. Mineral replacement reactions, In: Oelkers, E.H., Schott, J. (Eds.),
1202 Thermodynamics and Kinetics of Water-Rock Interaction. Mineralogical Society
1203 America, Washington, D.C., pp. 87-124.
1204 Putnis, C.V., Mezger, K.A., 2004, A mechanism of mineral replacement: Isotope tracing in
1205 the model system KCl-KBr-$H_2O$. Geochimica et Cosmochimica Acta 68, 2839-2848.
1206 Putnis, A., Putnis, C.V., 2007. The mechanism of reequilibration of solids in the presence of a
1207 fluid phase. Journal of Solid State Chemistry 180, 1783–1786.
1208 Putnis, A., Prieto, M., Fernandez-Diaz, L., 1995. Fluid supersaturation and crystallization in
1209 porous media. Geological Magazine 132, 1-13.
1210 Putnis, C., Tsukamoto, K., Nishimura, Y., 2005. Direct observations of pseudomorphism:
1211 compositional and textural evolution at a fluid-solid interface. American Mineralogist
1212 90, 1909-1912.
1213 Putnis, C.V., Geisler, T., Schmid-Beurmann, P., Stephan, T., Giampaolo, C., 2007. An
1214 experimental study of the replacement of leucite by analcime. American Mineralogist
1215 92, 19-26.
1216 Schiano, P., Provost, A., Clocchiatti, R., Faure, F., 2006. Transcrystalline melt migration and
1217 Earth's mantle. Science 314, 970-974.
1218 Schweda, P., Sjöberg, L., Södervall, U., 1997. Near-surface composition of acid-leached
1219 labradorite investigated by SIMS. Geochimica et Cosmochimica Acta 61, 1985-1994.
1220 Seyama, H., Soma, M., 2003. Surface-analytical studies on environmental and geochemical
1221 surface processes. Analytical Sciences 19, 487-497.
1222 Smets, B.M.J., Lommen, T.P.A., 1982, The leaching of sodium aluminosilicate glasses
1223 studied by secondary ion mass spectrometry. Physics and Chemistry of Glasses 23,
1224 83-87.
1225 Smith, J.V. Brown, W.L., 1988. Feldspar Minerals 1. Crystal Structures, Physical, Chemical
1226 and Microtextural Properties. Feldspar Minerals. Springer-Verlag, Berlin.
1227 Sposito, G., 1984. The Surface Chemistry of Soils. Oxford, New York.
1228 Stefánsson, A., Arnórsson, S., 2000. Feldspar saturation state in natural waters. Geochimica et
1229 Cosmochimica Acta 64, 2567-2584.
1230 Teng, H.H., Fenter, P., Cheng, L., Sturchio, N.C., 2001. Resolving orthoclase dissolution
1231 processes with atomic force microscopy and X-ray reflectivity. Geochimica et
1232 Cosmochimica Acta 65, 3459-3474.
1233 Tsomaia, N., Brantley, S.L., Hamilton, J.P., Pantano, C.G., Mueller, K.T., 2003. NMR
1234 evidence for formation of octahedral and tetrahedral Al and repolymerization of the Si
1235 network during dissolution of aluminosilicate glass and crystal. Geochimica et
1236 Cosmochimica Acta 88, 54-67.
1237 Velbel, M.A., 1993. Formation of protective surface layers during silicate-mineral weathering
1238 under well-leached, oxidizing conditions. American Mineralogist 78, 405-414.
1239 Wang, J., Kalinichev, A.G., Kirkpatrick, R.J., 2006. Effects of substrate structure and
1240 composition on the structure, dynamics, and energetics of water at mineral surfaces: A
1241 molecular dynamics modeling study. Geochimica et Cosmochimica Acta 70, 562-582.
1242 Weissbart, E.J., Rimstidt, J.D., 2000. Wollastonite: Incongruent dissolution and leached layer
1243 formation. Geochimica et Cosmochimica Acta 64, 4007-4016.

1244 Wirth, R., 2004. Focused Ion Beam (FIB): A novel technology for advanced application of
1245 micro- and nanoanalysis in geosciences and applied mineralogy. European Journal of
1246 Mineralogy 16, 863-876.
1247 Wirth, R., 2009. Focused Ion Beam (FIB) combined with SEM and TEM: Advanced
1248 analytical tools for studies of chemical composition, microstructure and crystal
1249 structure in geomaterials on a nanometre scale. Chemical Geology 261, 217-229.
1250 Wolery, T.J., 1992. EQ3NR, A Computer Program for Geochemical Aqueous Speciation-
1251 Solubility Calculations: Theoretical Manual, User's Guide, and Related
1252 Documentation (Version 7.0). Lawrence Livermore Natl. Lab. UCRL-MA-110662 PT
1253 III.
1254 Wollast, R., 1967. Kinetics of the alteration of K-feldspar in buffered solutions at low
1255 temperature. Geochimica et Cosmochimica Acta 31, 635-648.
1256 Wyart, J., Sabatier, G., 1958. Mobilité des ions des silicium et aluminium dans les cristaux de
1257 feldspath. Bulletin de la Societé française de Minéralogie et Cristallographie 81, 223-
1258 226.
1259 Yang, C., Samper, J., Zhu, C., Jones, S.B., 2009. Numerical modeling of the development of a
1260 preferentially leached layer on feldspar surfaces. Environmental Geology 57, 1639-
1261 1647.
1262 Zhang, L., Lüttge, A., 2009, Theoretical approach to evaluating plagioclase dissolution
1263 mechanisms. Geochimica et Cosmochimica Acta 73, 2832-2849.
1264 Zhu, C., Veblen, D.R., Blum, A.E., Chipera, S.J., 2006. Naturally weathered feldspar surfaces
1265 in the Navajo Sandstone aquifer, Black Mesa, Arizona: electron microscopic
1266 characterization. Geochimica et Cosmochimica Acta 70, 4600-4616.
1267

1268 **Figure Captions**

1269 Figure 1. Amorphous surface altered layer formed by leached layer mechanism (arbitrary
1270 scale, view in cross section). The anticorrelated, sigmoidal concentration profiles are created
1271 by solid-state volume interdiffusion of preferentially released cations (cation profile- white)
1272 with protons from bulk solution (H profile- black)- this represents the core process. The
1273 leached layer is a relict structure bonded to the unaltered mineral; the thickness is controlled
1274 by two rates: diffusion (inner interface) and surface chemical reactions (outer interface); when
1275 the inner and outer interfaces move at the same rate, the layer thickness becomes constant.
1276 Leached layers may undergo structural reorganization reactions such as condensation and
1277 densification (see text for details).
1278

1279 Figure 2. High-resolution TEM structural images, chemical maps, and cation depth profiles of
1280 surface layers formed on silicate minerals after laboratory (A-C) and field chemical
1281 weathering (D, E). A: labradorite : (i) BF TEM image with EDX profiles (dark ovals = C
1282 contamination from EDX), H SIMS profile in inset (true H profile is sharper-see text); (ii)

HRTEM image; EFTEM chemical maps with Ca (iii) and Si (iv) profiles (Si map obtained in different location, faint white areas in feldspar are an artifact). B: wollastonite: (i) BF TEM image, note fluid-filled pores and physical separation of surface layer from wollastonite (elongated white zone), insets show EFTEM Si and Ca profiles; (ii) AFM image of surface. C: pyrope garnet: HRTEM image, inset shows EDX-cation profiles (inset from different location; true chemical gradients are sharper because of EDX-beam broadening). D: K-feldspar: HRTEM image, superposed EFTEM K profile. E: serpentine: EDX chemical map-Mg (yellow), Si (green), Si-rich and Mg-poor surface layer (dark green), lichen (grey, hole = black).

Figure 3. Interdiffusion modeling of binary cation-proton exchange, simulating leached layers. **(**A**)** Variation of binary interdiffusion coefficient log $D_\alpha$ as a function of normalized cation concentration (proportional to depth) and structural factor $\alpha$. **(**B**)** Normalized cation concentrations as a function of depth into the altered layer based on univalent (binary) cation-proton interdiffusion (only cation profiles shown). Curves based on $\alpha = -0.9$, $a = 10^{-2}$ Å $s^{-1}$, $D_H$ ($H^+$ or $H_3O^+$ diffusion coefficient), and $D_H / D_{cation}$ ($10^{-2}$, $10^{-3}$, $10^{-4}$, $10^{-5}$; corresponding profiles left to right for each value of $D_H$). Overall, these diffusion curves demonstrate that an interdiffusion process (leached layer mechanism) is not compatible with thick altered surface layers (> 20 nm) having sharp chemical boundaries. (C) Simulated binary, multivalent cation-$H^+$ ($H_3O^+$) interdiffusion. Cation depth profiles as a function of $\alpha = -0.9$, $a = 10^{-2}$ Å $s^{-1}$, $D_H$ ($H^+$ or $H_3O^+$ diffusion coefficient), $D_H / D_{cation} = 10^{-3}$, and cation valence ($z$). The individual, binary cation depth profiles start to increasingly diverge as a function of valence when $D_H \geq 10^{-14}$ $cm^2$ $s^{-1}$, showing strong dependence of cation depletion depths on valence (see text for details).

Figure 4. Coupled interfacial dissolution-reprecipitation mechanism (top), and general concept of chemical weathering continuum (bottom). Cross sectional view of surface layer

separated from crystalline parent mineral by a thin fluid film. Chemical reactions control stoichiometric release of elements from mineral (inner interface) to thin fluid film; this is coupled to precipitation of an amorphous, silica-rich surface layer (light grey); step function-like depletions in certain cation concentrations- yellow dashed line; partial retention of cations- yellow arrow). Stoichiometric chemical reactions control the release of elements at outer interface. The continuum concept of chemical weathering, based solely on the interfacial dissolution-reprecipitation mechanism, has two end-members defined by the nature of the precipitated phase. This serves to integrate our results, based on the precipitation of amorphous silica, with mineral replacement reactions, into a continuum concept that encompasses both laboratory and natural chemical weathering.

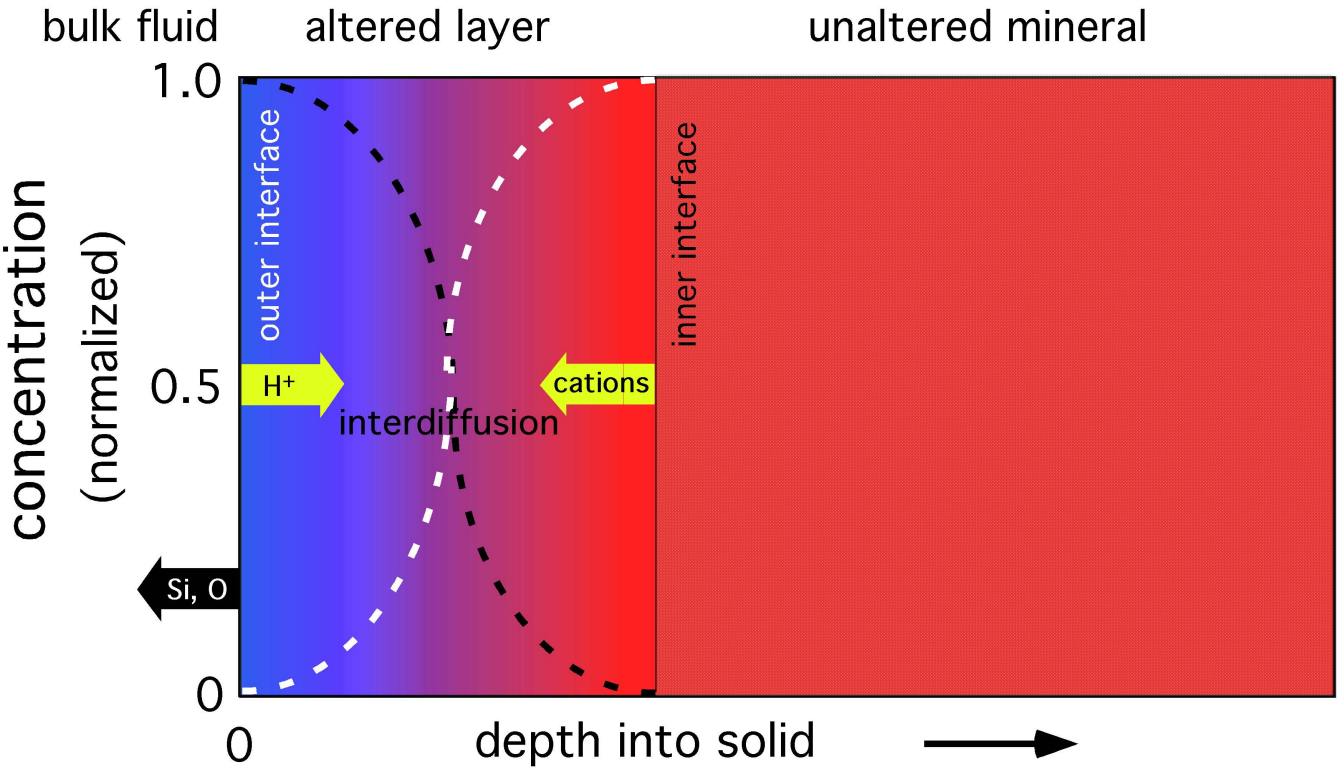


Fig. 1 Hellmann et al.

note: the final printed size should not be less than 50% of the above size

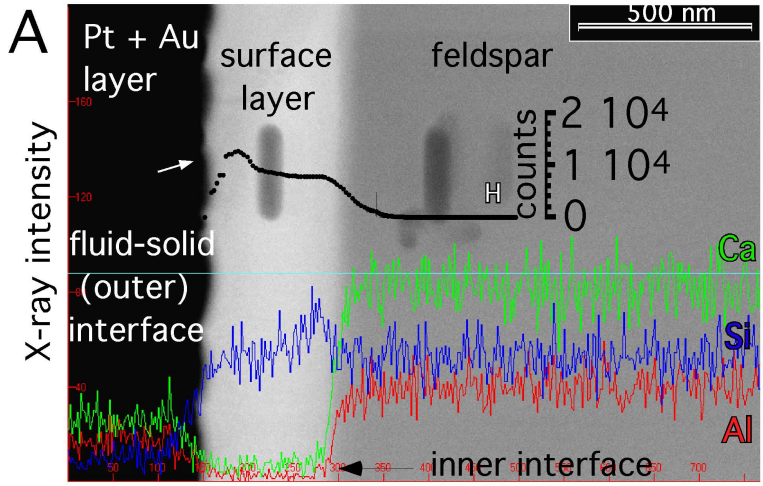


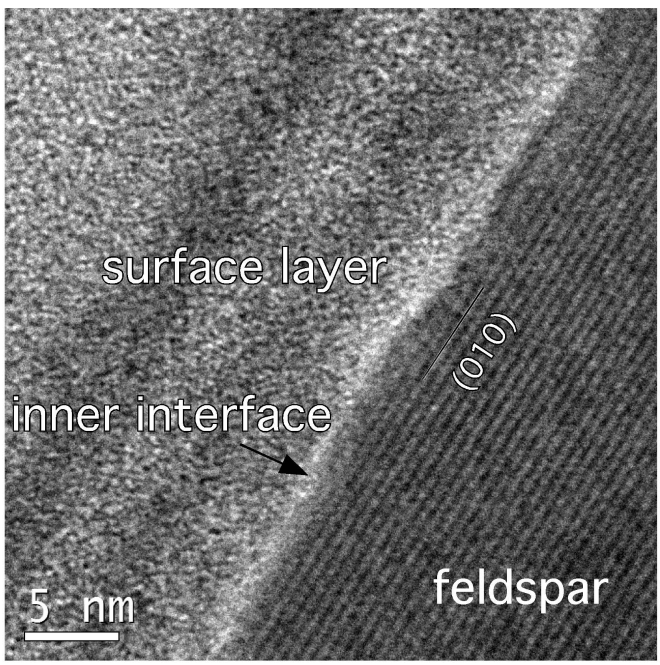


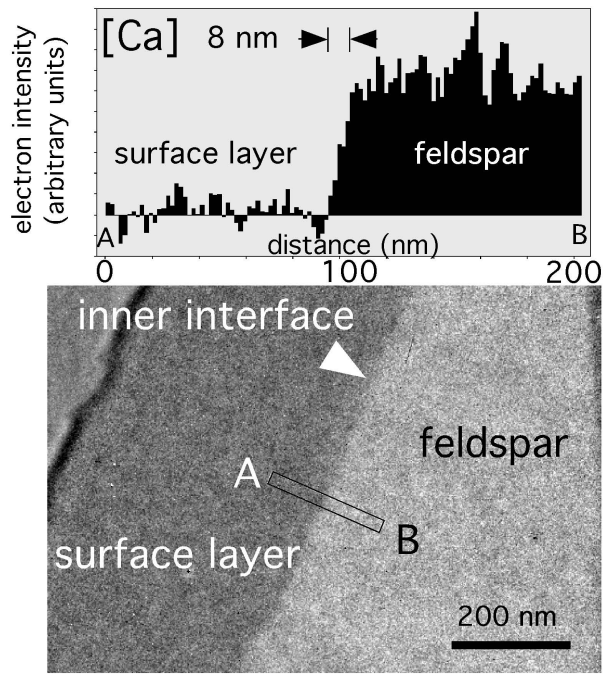


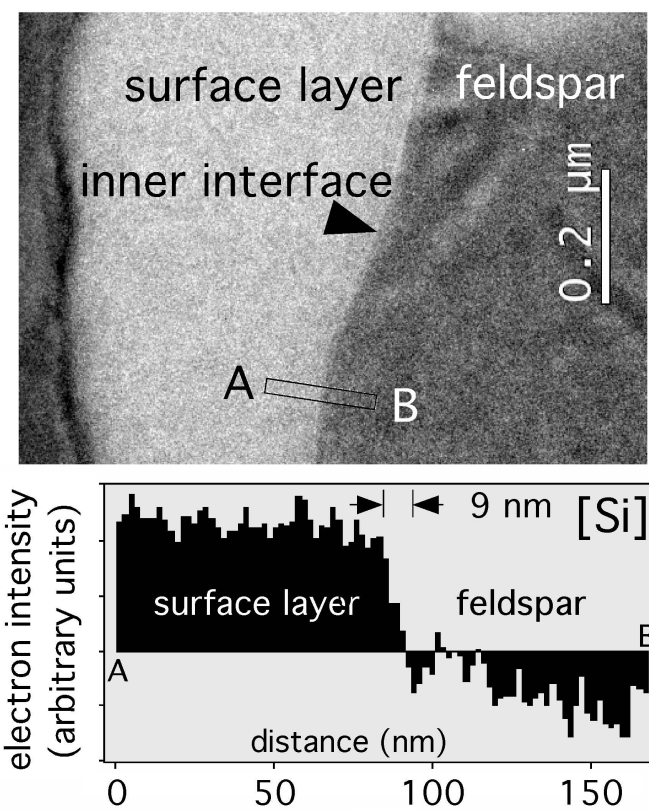


Figure 2A, Hellmann et al.

printed size- not less than 50%

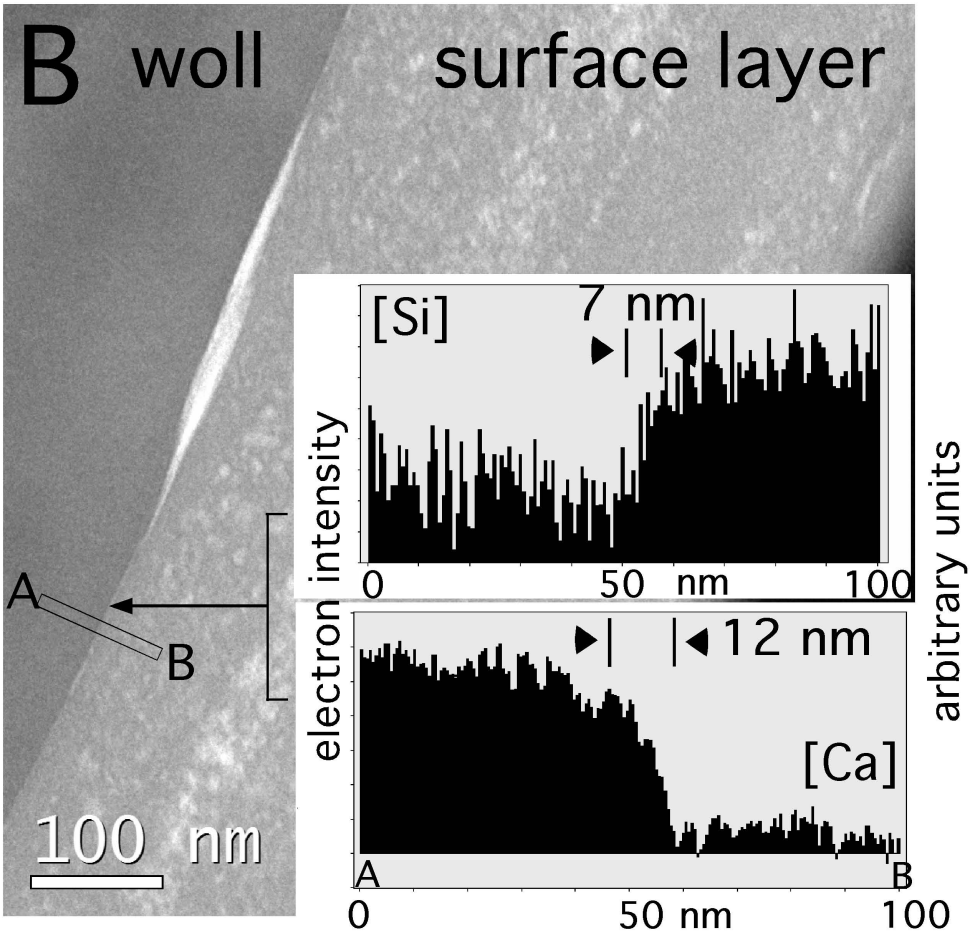


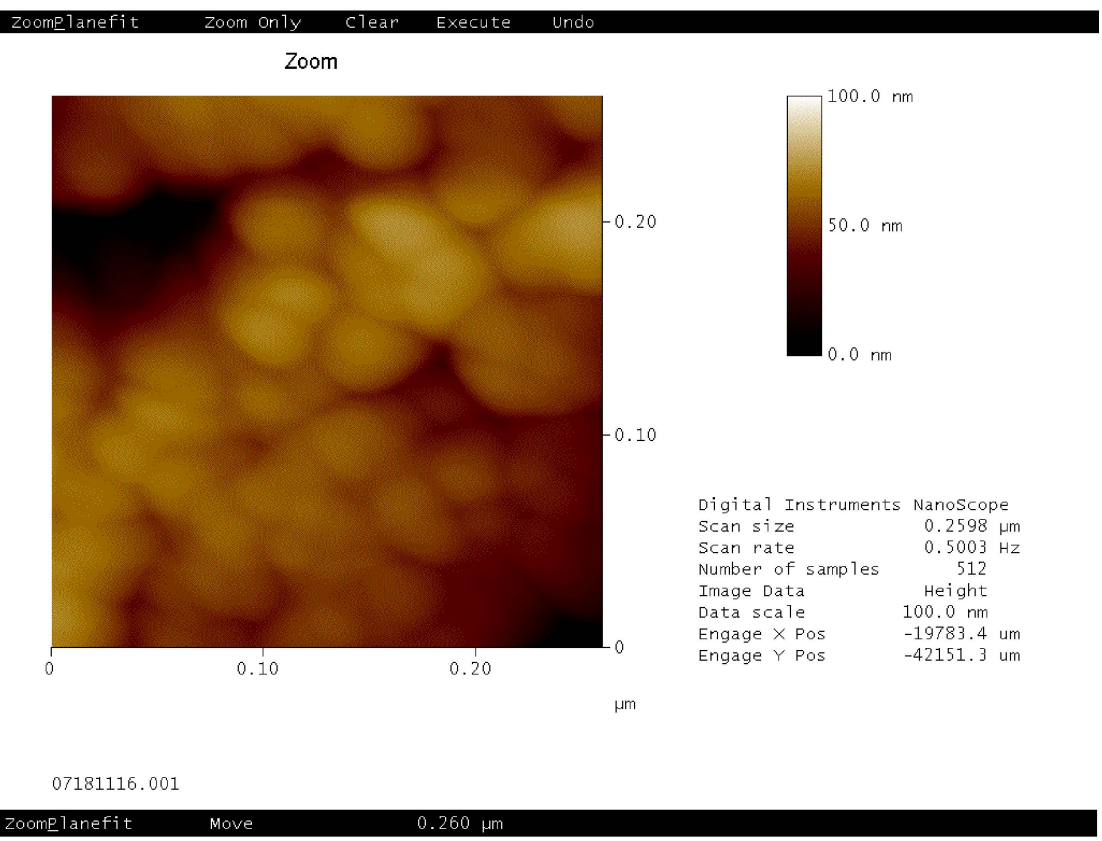


Figure 2B, Hellmann et al.

final printed size not less than 50% of above size

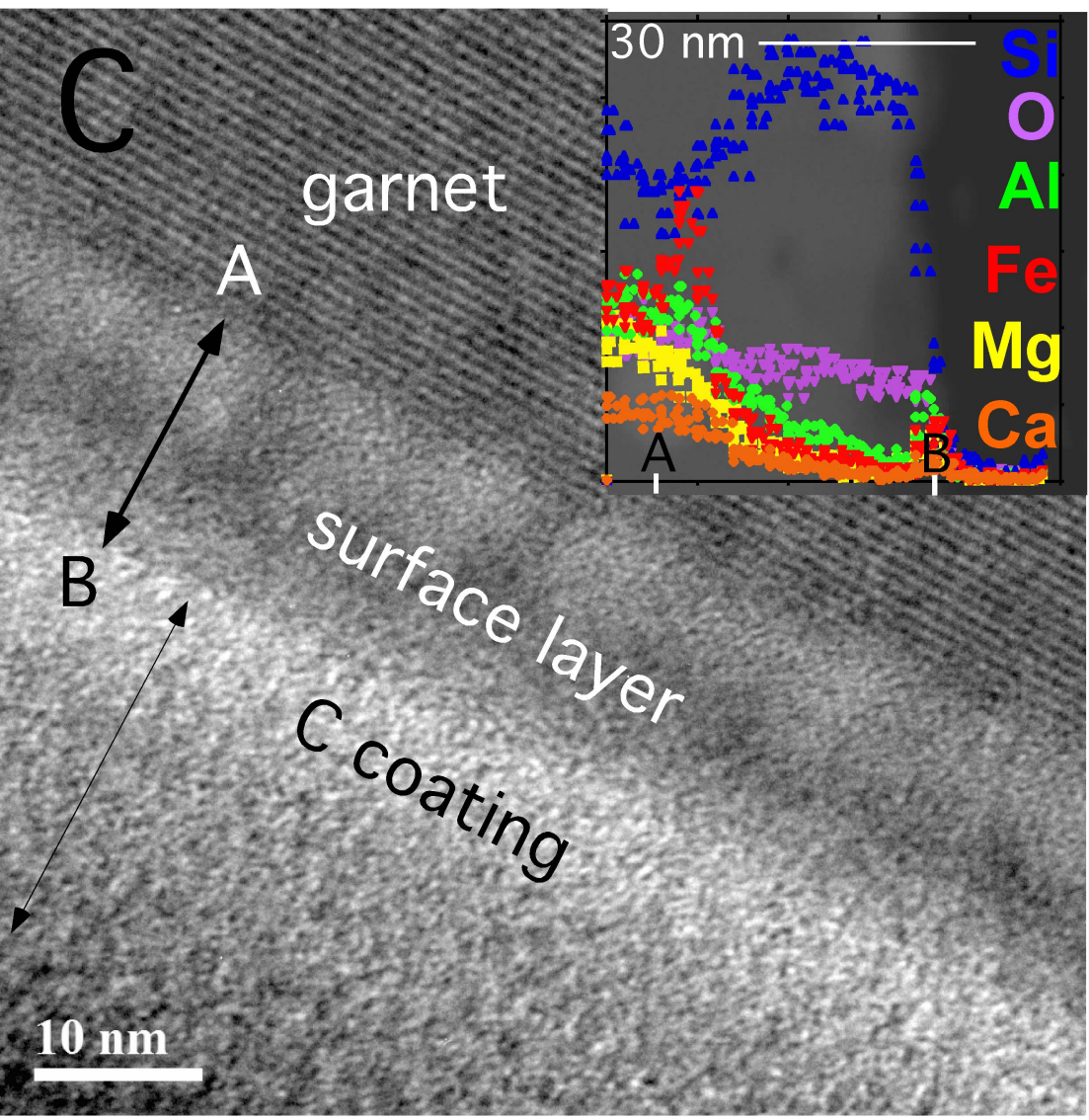


Figure 2C, Hellmann et al.

final printed size not less than 50% of above size

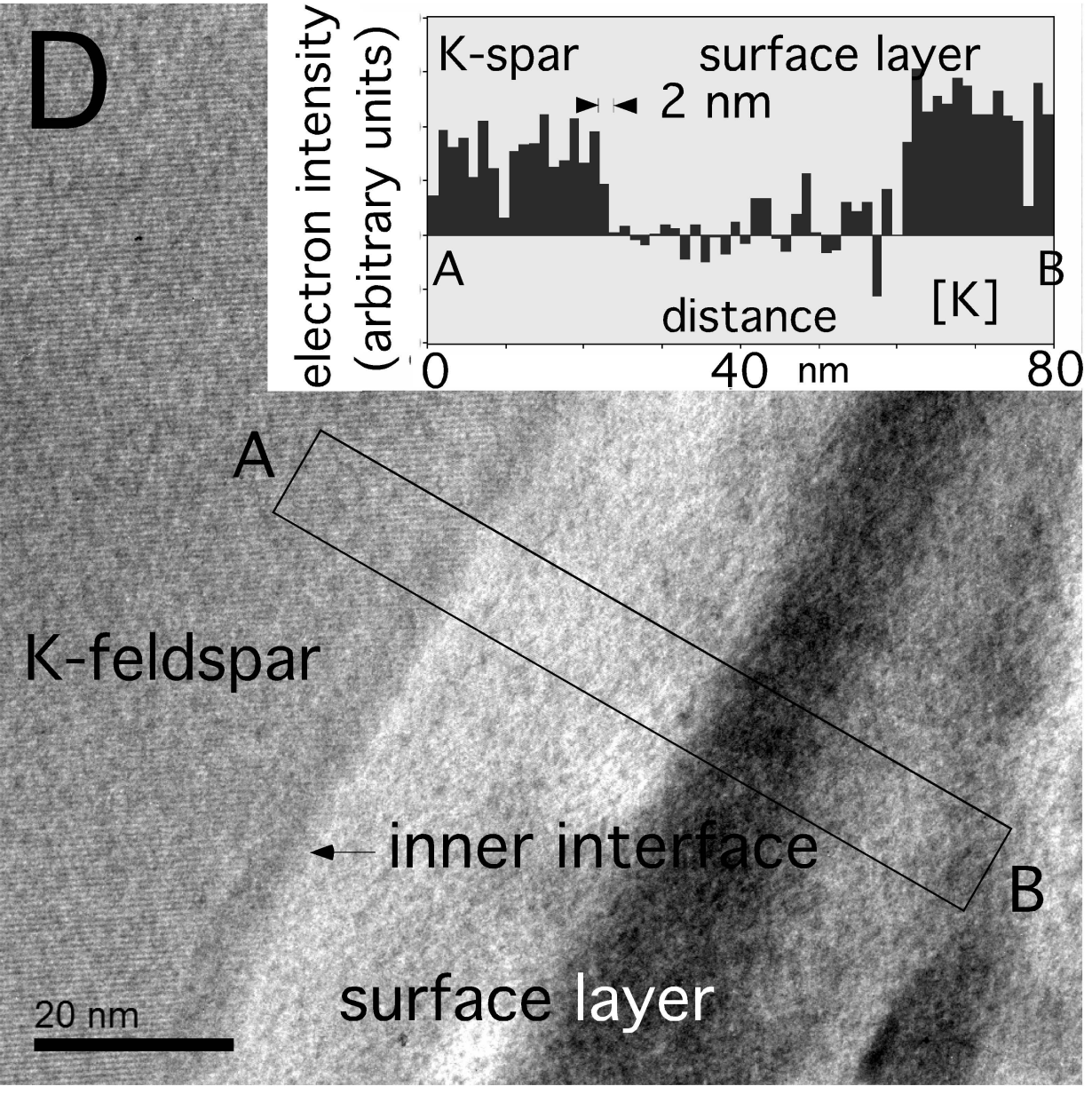


Figure 2D, Hellmann et al.

final printed size not less than 50% of above size

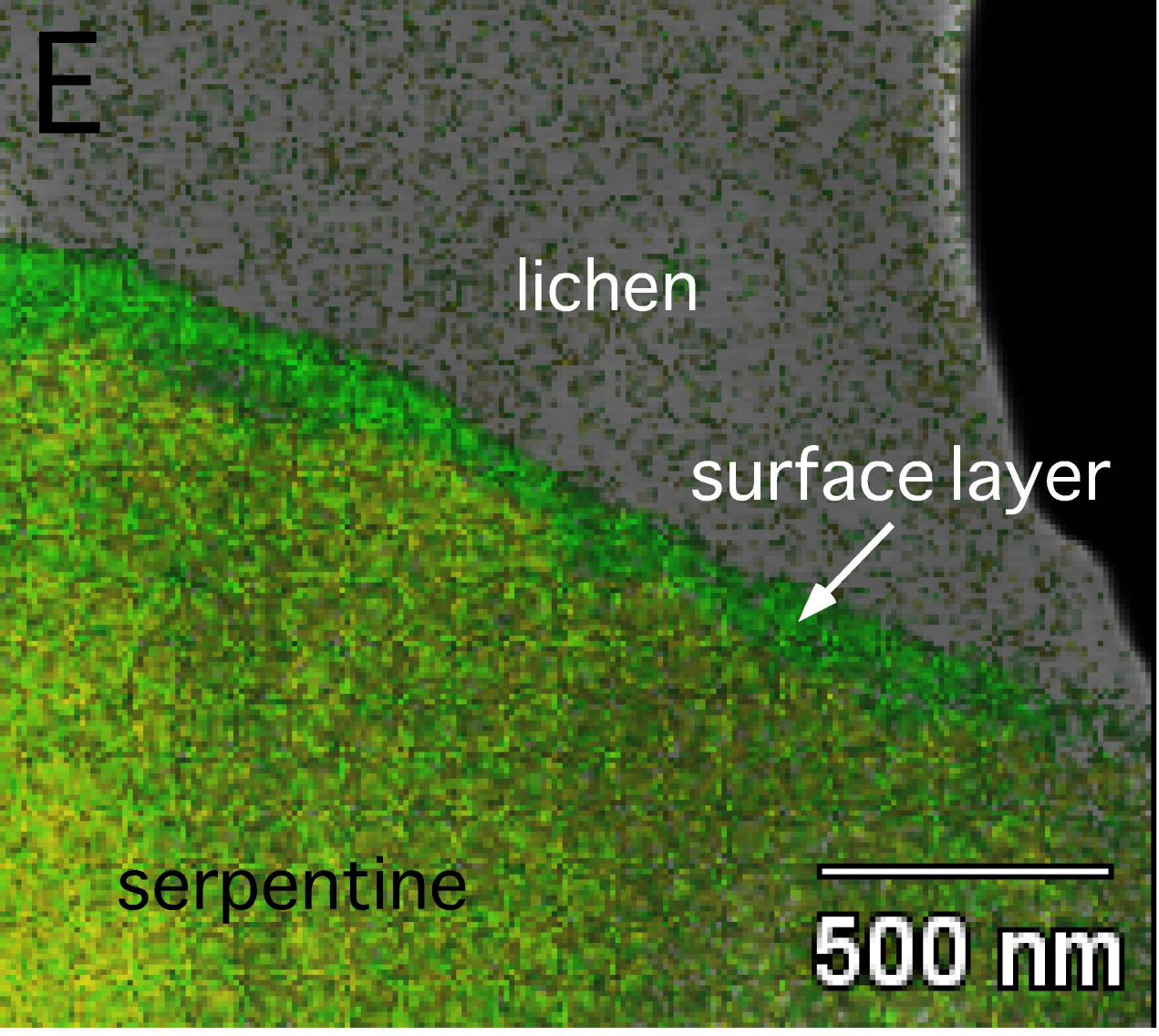


Fig. 2E, Hellmann et al.

final printed size not less than 50% of above size

**A**

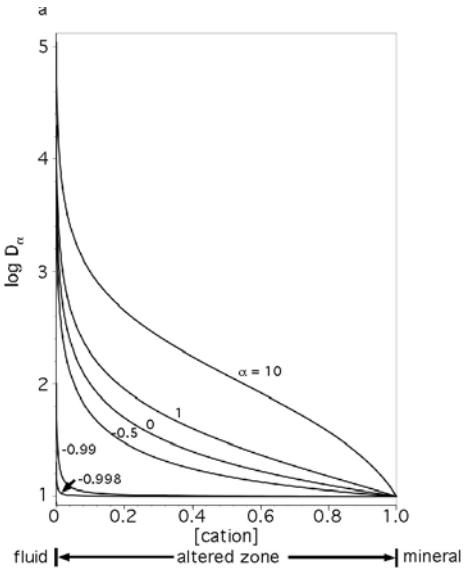


**B**

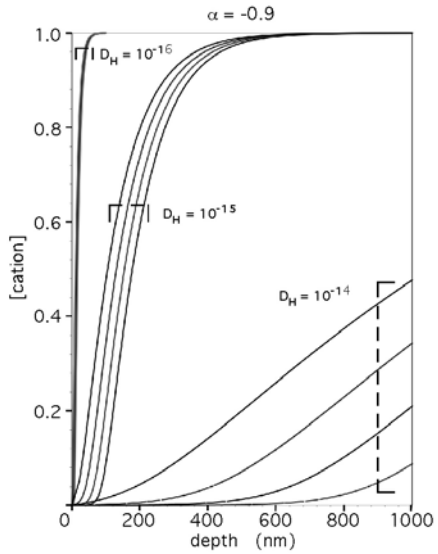


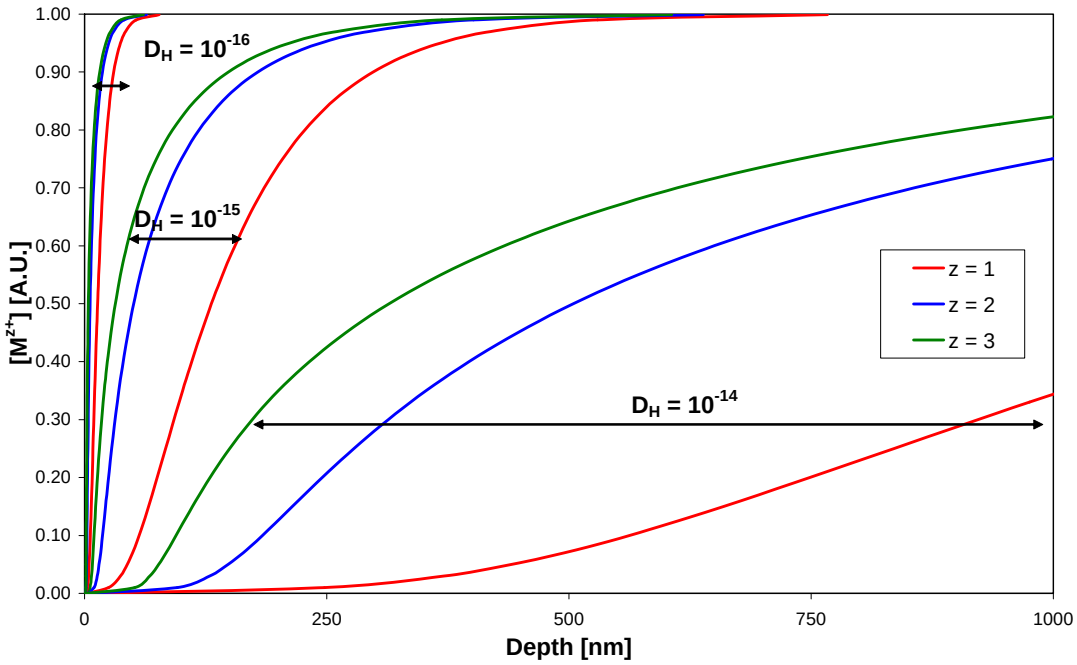


**C**

Figure 3, Hellmann et al.

| |
|---|
| final printed size same as above for A, B, and C |

Fig. 4

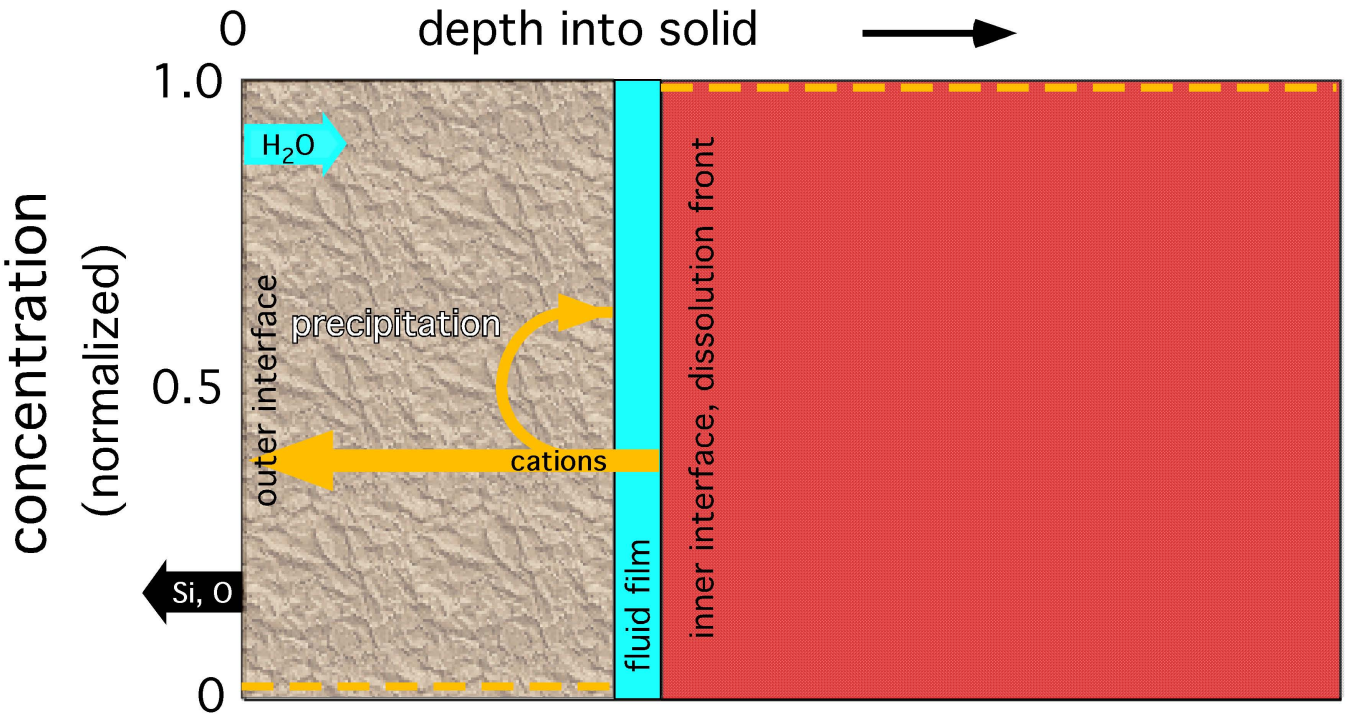


bulk fluid surface layer unaltered mineral

chemical weathering continuum

| | | |
|---|---|---|
| amorphous precipitates | amorphous precipitates + crystalline phases | mineral-mineral replacement |

Hellmann et al.

final printed size not less than 50% of above size